University of Tokyo
Graduate School of Science
Department of Physics

Study on the effect of supernova fallback on the neutron star diversity
(超新星フォールバック降着によって発現する中性子星の多様性)

Yici ZHONG (鐘伊慈)

A thesis submitted to
the graduate school of science,
the University of Tokyo
in partial fulfillment of
the requirements for the degree
of
Master of Science in Physics

August 11, 2021

Abstract

Neutron stars (NSs) are compact stellar objects with a mass of 1-2 $M_\odot$ and a radius of ~ 10 km. They are mainly formed in a gravitational collapse of a massive star with an initial mass of $\gtrsim 10\,M_\odot$ and an iron core. Young isolated NSs in the Galaxy can be divided into three categories primarily depending on the energy source for the emission: rotation-powered pulsars (RPPs) that are mainly powered by rotational energy, magnetars that are mainly powered by magnetic field energy, and central compact objects (CCOs) that are mainly powered by latent heat. The most significant difference among them is the surface magnetic field B_*; it is considered to be $\sim 10^{12-13}$ G, $\gtrsim 10^{14}$ G, and $\lesssim 10^{11}$ G for RPPs, magnetars and CCOs, respectively. The origin for this diversity is unsettled.

One process that may account for this diversity is the supernova fallback accretion. A tail part of marginally bound matter ejected with the supernova explosion falls back to the newborn NS after the neutrino luminosity significantly decreases. The fallback matter encounters with an outflow from the nascent magnetosphere, which could induce the trifurcation of NSs into RPPs, CCOs, and magnetars. If the outflow repels the fallback accretion, a RPPs with clean magnetosphere may form. Otherwise the magnetosphere will be disturbed or even buried, which leads to the formation of magnetars with synthesized multi-pole magnetic field and CCOs with apparently weak magnetic field, respectively.

In this thesis, we numerically investigate the dynamics of a supernova fallback accretion confronting with a relativistic wind from a newborn NS through one dimensional relativistic hydrodynamics simulation, and find that the time evolution of the accretion shock in the radial direction is basically characterized by the encounter radius of the in- and outflow $r_{\rm enc}$ and a dimensionless parameter $\zeta \equiv L/\dot{M}_{\rm fb}c^2$, where L is the NS wind luminosity and $\dot{M}_{\rm fb}$ is the fallback mass accretion rate. We find that the critical condition for the fallback matter to reach near the NS surface can be simply described as $\zeta < \zeta_{\rm min} \equiv GM_*/c^2 r_{\rm enc}$ independent of the outflow Lorentz factor, with M_* being the NS mass. With combining the condition for the fallback matter to bury the surface magnetic field under the NS crust, we find that the trifurcation of NSs into RPPs, CCOs, and magnetars occurs for the case with the surface magnetic field $B_{*,\rm tri} \sim$ a few 10^{13} G and rotation period $P_{\rm i,tri} \sim O(10)$ ms. Since such a NS formation is considered to be typical, our scenario can naturally explain the observed fact that the formation rate of RPPs is roughly comparable to those of CCOs and magnetars.

Acknowledgements

First and foremost, I would like to express my deepest gratitude towards my supervisor, Prof. Naoki Yoshida, who officially guided me to the world of astrophysics when I was a naive "dreamer" who have been interested in the physics the most but spent half of the college life fighting with the engineering textbooks; I always felt grateful for your kindly guidance and useful suggestions, in which I have not only learnt about the academic stuff I need to thrive, but also about how to enjoy the life in Tokyo. Dr. Kazumi Kashiyama, my greatest mentor and closest collaborator, who has tolerated my stupid questions and naive thoughts for a long time and taught me almost everything about my current research topic both from the side of theory and numerical simulation, thanks for your constant encouragement and assistance; I have never thought about that I can use C++ to actually do something after I almost failed this course during my undergraduate. Sincerely hope that HUNTER $\times$ HUNTER would be updated periodically instead of sporadically in the near future.

I would like to thank all my other collaborators; Prof. Toshikazu Shigeyama showed me the way of thinking and model construction as a well-trained physicist, and Dr. Shinsuke Takasao provided numerous technical suggestions on the numerical simulations. I also want to thank my secondary supervisor in the program of IGPEES, Prof. Masahiro Ikoma and Prof. Takanobu Amano, who has spent their precious time reading/listening to my naive research proposal and provide the insightful thoughts from different fields. To all of the UTAP-RESCEU members, thanks for the help both on physics and daily life; especially Tarumi-san and Kana-san, my poor Japanese can not be improved without you two. I also want to thank UTAP-clusters and Yukawa Institute for Theoretical Physics for the technical resources. Besides, special thanks shall be given to C.K., who broadly extended my interests to the social science; and Akutami Gege, who invents two of my favorite characters, Gojo Satoru and Geto Suguru; I really enjoyed the beautiful symmetry existed in their love story.

Finally, I want to thank my parents for their understanding and support, which is really important for me.

This work is supported by International Graduate Program for Excellence in Earth-Space Science (IGPEES) at the University of Tokyo.

Contents

List of Tables

List of Figures

Chapter 1

Introduction

Neutron stars are compact stellar remnants that mainly form at the center of a collapsing massive star with zero-age main sequence (ZAMS) mass $M_{\rm ZAMS} \gtrsim 10 M_\odot$ (Heger et al., 2003) and iron cores at the last stage of the stellar evolution accompanied by a supernova (SN) explosion [1]. The mass ejected during this process forms an expanding shell named supernova remnant (SNR), and a pulsar wind nebula (PWN) can be found inside the shell. Density of NSs can be estimated by their typical mass $M_* \sim 1.4 M_\odot$ and typical radius $R_* \sim 12$ km as $\sim 4 \times 10^{14}$ g cm^{-3}, which is even higher than the mass density of nucleon matter and the general relativistic effects will be non-negligible especially in the inner region with high matter energy density. Together with white dwarfs and black holes, they are called compact objects; NSs serve as a unique laboratory to probe fundamental physics (e.g., general relativity and nuclear matter physics) as a combination of the extreme gravity, magnetism and density. It is also important to understand their astrophysical nature such as formation mechanism and diversity.

In this chapter, we will briefly introduce the general characteristics of NSs in Sec. 1.1, while presenting the unique properties of three subclasses among young NSs (rotation-powered pulsars, magnetars and central compact objects) in Sec. 1.2. Sec. 1.3 is devoted to consider possible mechanisms that can induce the diversity of young NSs and how it motivates our work done in the following part of this thesis.

1.1 Fundamental properties of neutron star

There are several physical quantities that can parameterize an NS: surface temperature T_* given by spectra, and stellar rotation period P_i and period derivative $\dot{P}_i$ obtained from the light curve. Temperature mainly provides the information of surface radiation, superfluidity, interior composition and etc (e.g., Lattimer & Prakash, 2007; Tsuruta et al., 2009; Lattimer, 2012; Potekhin et al., 2015). The surface magnetic field strength B_*, which mainly controls the motion of plasma and emission geometry, can be derived from the rotation period P_i and its secular period derivative $\dot{P}_i$ in canonical pulsar models that proposes the NS as a rotating

[1] Note that there are alternative ways to form an NS other than this; e.g., binary NS mergers (e.g., Hotokezaka et al., 2013) and accretion-induced collapse of a white dwarf (e.g., Nobili et al., 2008; Enoto et al., 2014); where the latter one generally lead to the formation of Type Ia SN.

magnetic dipole supported by rotational energy (e.g., Goldreich & Julian, 1969). Given the spin angular frequency as

$$\Omega_i = 2\pi/P_i, \tag{1.1}$$

the rotation energy of a NS can be written as

$$E_{\rm rot} = \frac{1}{2} I \Omega_i^2 \tag{1.2}$$

where I stands for the moment of inertia of the NS, and can be written as follows if we consider it to be spherically symmetric

$$I = \frac{2 M_* R_*^2}{5}, \tag{1.3}$$

where the flux of rotational energy losing (i.e., the spin-down luminosity) can be written as

$$L_{\rm sd} = -\frac{{\rm d}E_{\rm rot}}{{\rm d}t} = \frac{4\pi^2 I \dot{P}_i}{P_i^3}. \tag{1.4}$$

On the other hand, the Poynting flux from a rotating sphere with dipole magnetic field is shown as

$$L_{\rm dp} = \frac{B_*^2 \Omega_i^4 R_*^6}{6c^3}. \tag{1.5}$$

The dependence of dipole magnetic field strength B_* on rotation period P_i and period derivative $\dot{P}_i$ can be obtained while considering

$$L_{\rm sd} = L_{\rm dp} \tag{1.6}$$

as

$$B_* = \sqrt{\frac{3c^3 I}{2\pi^2 R_*^6} P_i \dot{P}_i} = 1.0 \times 10^{14} {\rm G} \left(\frac{P_i}{1\ {\rm s}} \right)^{1/2} \left(\frac{\dot{P}_i}{10^{-11} {\rm s\ s^{-1}}} \right)^{1/2}. \tag{1.7}$$

Thus

$$P_i \dot{P}_i = \frac{2\pi^2 R_*^6 B_*^2}{3c^3 I} = {\rm const}, \tag{1.8}$$

and since

$$\int_0^{\tau_{\rm c}} (P_i \dot{P}_i) dt = \int_{P_0}^{P} P_i dP_i, \tag{1.9}$$

where P_0 is the initial rotational period of the NS, we have

$$\frac{P^2 - P_0^2}{2} = P \dot{P} \tau_{\rm c} \tag{1.10}$$

which gives the spin-down characteristic-age $\tau_{\rm c}$ of the NS as

$$\tau_{\rm c} \sim \frac{P}{2\dot{P}}. \tag{1.11}$$

Eq.(1.11) can be used to estimate the age of NS $t_{\rm age}$ at the limit of $P_0^2 \ll P^2$ [2].

[2]The other way to measure the age, type, progenitors and birth environment of a NS is through the size and expanding velocity of their associated SNRs, which are bright in x-ray band for $\lesssim 10$ kyr (i.e. this method is only valid for young NSs). The kinematic age from the proper motion of the targets and energetics of their associated pulsar wind nebulae (PWNe) can also used to determined the age of the NSs (Enoto et al., 2019).

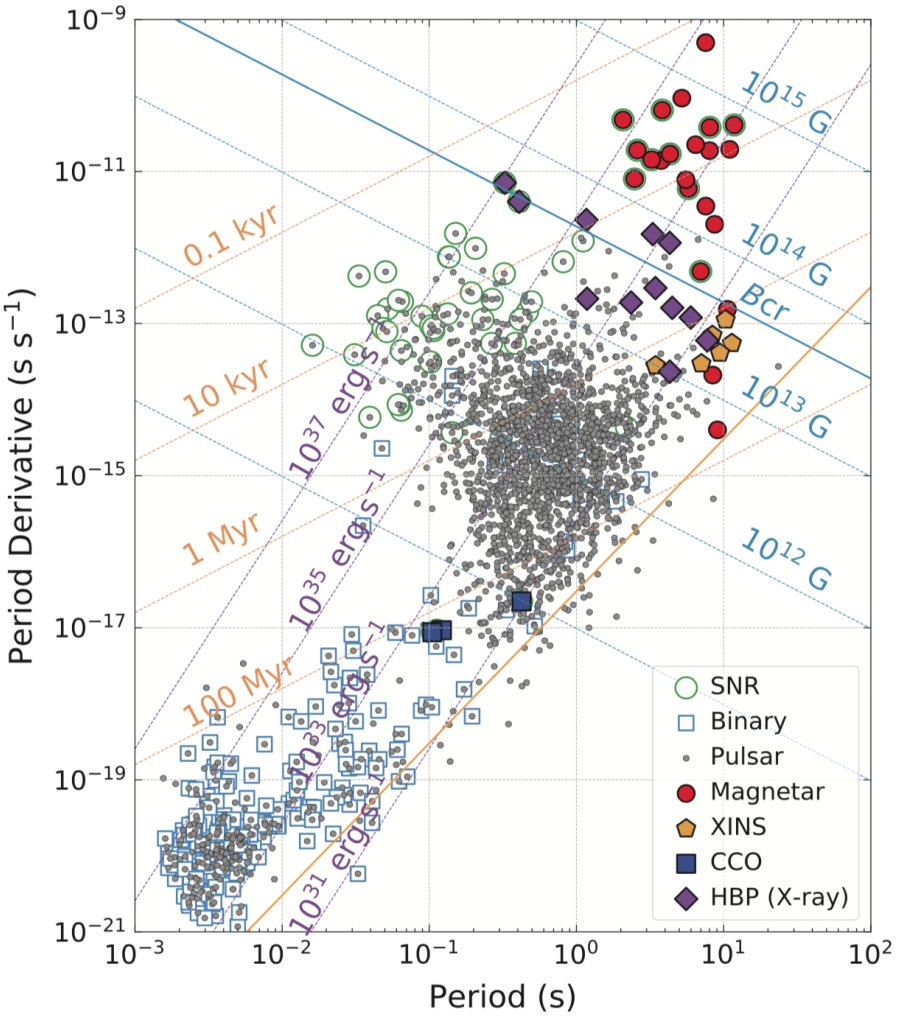

Figure 1.1: Repost from the fig.1 in Enoto et al. (2019): P_i-$\dot{P}_i$ (period and period derivative plane) diagram of known NSs: high-B pulsars with x-ray emission reported (HBP, purple diamonds), x-ray isolated neutrons stars (XINSs, orange pentagons), pulsars (grey dots), magnetars (red filled circles), and compact central objects (CCOs, blue filled squares). Additional marks are added if one is found in a binary system (blue open square) or associated with a supernova remnant (SNR, see green open circle). The data are taken from the McGill magnetar catalogue and Australia Telescope National Facility (ATNF) pulsar catalogue (version 1.60) for magnetars and pulsars, respectively (e.g., Manchester et al., 2005; Olausen & Kaspi, 2014); and the sources of HBPs, XINSs, and CCOs are mainly based on Zhu et al. (2011), Fesen et al. (2012), Olausen et al. (2013) and the references therein. The surface magnetic fields B, characteristic age τ_c and spin-down luminosity L_{sd} are overlaid in cyan, orange and purple dashed lines, respectively. One of the theoretical death-lines (e.g., from Eq.(6) of Chen & Ruderman, 1993) and the critical field $B_{cr} = 4.4 \times 10^{13}$ G and are shown in orange and cyan solid straight lines, respectively.

The spin-down characteristic age of different categories of NSs are shown as orange dashed lines in P_i-$\dot{P}_i$ phase diagram (see Fig. 1.1); in which the one of pulsars are mainly estimated from their radio band as $\lesssim$ 100 Myr (see the grey solid points) except for a portion called millisecond pulsars (MSPs) with $\sim 80\%$ locating in the binary system (see the grey solid points with blue open circle at the lower-left corner with $P_i \sim O(1)$ ms); they are considered to spin down for $\sim$ 10 Myr and then spun up by accretion from their binary companion (e.g., Alpar et al., 1982). Young magnetized NSs associated with PWNs and SNRs of ages $t_{\rm age} \lesssim$ 1-10 kyr were considered to be born at the upper-left corner and move right and downwards as they age, where this moving direction is determined by the braking index n in the general spin-down relation:

$$\dot{\Omega}_i = -k\Omega_i^n \tag{1.12}$$

which is being taken as 3 here in the case of magnetic dipole radiation [3]. The radio emission of pulsars will cease at at the lower-right corner (see the orange solid straight line in Fig. 1.1 for reference), which defines the so-called death-lines of pulsars. Generally speaking, this shall be related to the radiation processes around the magnetosphere of NSs (e.g., synclotron radiation and absorption, two-photon pair creation and annihilation, Bremsstrahlung), with the boundary defined as the light cylinder r_{lc} by assuming the co-rotation velocity of particles and magnetic field to be the speed of light c

$$r_{\rm lc} = c/\Omega_i \sim 3.0 \times 10^8\,{\rm cm}\,{\Omega_{\rm i,-2}}^{-1}, \tag{1.13}$$

where the closed magnetic field line around the NS becomes open. The foot-points on the NS surface of the open/close boundary defines the so-called polar cap, and the particles flowing along them carry a bulk of Poynting flux and become the pulsar wind. Inside the light cylinder, the strong electric fields generated by rotating dipole

$$\mathbf{E} = -\frac{\mathbf{\Omega} \times \mathbf{r}}{c} \times \mathbf{B} \tag{1.14}$$

pulls charges out of the NS surface to fill the magnetosphere (e.g., Goldreich & Julian, 1969). The scale for the current density to flow along the open field lines can be determined through assuming that the charge density is large enough to screen the electric field along the magnetic field lines

$$\rho_{\rm m} \simeq -\frac{\mathbf{\Omega} \cdot \mathbf{B}}{2\pi c}. \tag{1.15}$$

However, if the charge density satisfied Eq. (1.15) in the entire region of magnetosphere, the induced $\mathbf{E} \cdot \hat{B}$ with $\hat{B}$ to be the unit vector of magnetic field $\mathbf{B}$ will not accelerate the particles to redistribute the charge density. In this sense, the theories accounting for the emission mechanism are generally trying to address the problem of where and how the charge density deviates from $\rho_{\rm m}$. To the upper end, the charged particles can be accelerated by the maximum electric potential drop for rotating dipole field (e.g., Ruderman & Sutherland, 1975)

$$\Delta V_{\rm max} \approx \frac{B_* R_*^3 \Omega_i^2}{2c^2}, \tag{1.16}$$

[3] However one shall notice that this braking index is not observed to be 3 for most of the pulsars ($2.8 > n > 1$, e.g., see Hamil et al., 2015), which may be explained through considering different emission mechanisms: e.g., $n = 1$ for particle wind braking, n=5 for a gravitational wave braking according to Shapiro & Teukolsky (1983); superfluidity and superconductivity of the matter within pulsars (e.g., Sedrakian & Cordes, 1998) and so on.

to the Lorentz factor

$$\Gamma_e = \frac{e\Delta V_{\rm max}}{m_e c^2} \tag{1.17}$$

with e and m_e to be the charge and mass of electron, which leads to the curvature radiation with characteristic frequency of $\Gamma_e^3 c/r_c$, where r_c is the curvature radius of the magnetic field line. In order to produce the electron-positron pairs as

$$\gamma + B \rightarrow e^- + e^+ \tag{1.18}$$

with B being the magnetic field (Sturrock, 1971),

$$\Gamma_e^3 \frac{\hbar c/r_c}{2m_e c^2} \frac{B_\perp}{B_{\rm cr}} \gtrsim \frac{1}{15} \tag{1.19}$$

shall be satisfied (Chen & Ruderman, 1993), with $B_{\rm cr}$ and $B_\perp$ being the quantum critical field (see Eq. (1.22)) and

$$B_\perp \approx \frac{B_*}{r_c}\sqrt{\frac{R_*^3\Omega_i}{c}}. \tag{1.20}$$

The death-line of pulsars is mainly considered to be achieved when the maximum electric potential in the acceleration region is insufficient to accelerate the charged particles to the threshold energy for the pair production to happen.

1.2 Diversity of young neutron star

In the phase diagram of NS rotation period P_i and surface magnetic field B_* as shown in Fig. 1.2, young isolated NSs can be mainly categorized into three classes with different energy source based on the multi-wavelength information: rotation-powered pulsars (RPPs) that are powered by spin-down energy loss (see Sec. 1.2.1), magnetars that are powered by magnetic field energy (see Sec. 1.2.2) and central compact objects (CCOs, see 1.2.3) that are powered by residual heat (e.g., Woods & Thompson, 2006; Enoto et al., 2019) .

1.2.1 Rotation-powered pulsars

The first signal being detected from the NS came from RPPs, which has rotation periods $\sim$ 0.01-1 s. They mainly lose rotation energy through ejecting energetic particles to their surrounding pulsar wind nebulae (PWN) and pulsates in a remarkably regular way (e.g., Hewish et al., 1968). RPPs were primarily detected in radio band [4], while their energy spectrum broadly extends to optical, x-ray and γ-ray band, in which the thermal blackbody emission lies between optical and soft x-ray band, and non-thermal power-law emission can be observed in γ-ray or radio band (e.g., incoherent component in infrared and γ-ray band and coherent component in radio band). Regardless of the effect of NS atmosphere, the thermal emission spectrum mainly produced by the residue cooling can potentially be used for constraining the equation of state of RPPs by comparing their temperatures and luminosities with the theoretical cooling curves.

[4]This once gives their name as radio pulsars; however information from some band may get lost due to the beaming direction, which makes it more scientifically reasonable to name RPPs with their energy source.

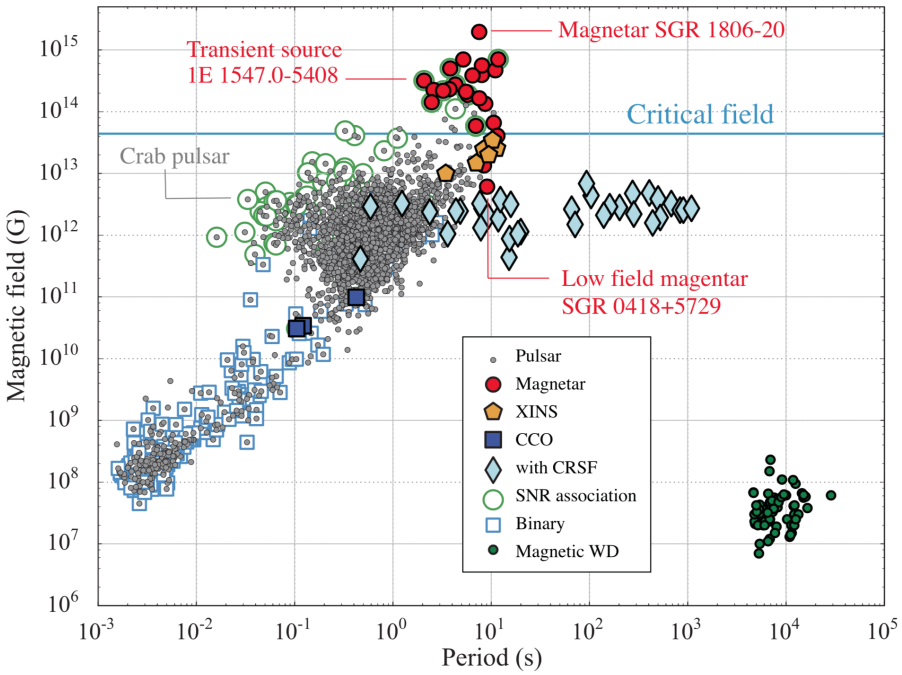

Figure 1.2: Repost from the Fig. 5 in Enoto et al. (2019); the phase diagram of P_i and B_* (rotation period and surface magnetic field) of different types of NSs. Accreting x-ray pulsars and the x-ray spectra of which exhibit cyclotron resonance scattering feature (CRSFs) taken from Staubert, R. et al. (2019) are also included. The magnetic white dwarfs (WDs) from Ferrario et al. (2015) are shown for comparison.

On the other hand, the non-thermal radiation of RPPs, which serves as a probe for the particle acceleration and pair-cascade mechanism in RPPs magnetosphere, is considered to come from the particles that are accelerated by electric fields parallel to the magnetic fields near the polar caps (e.g., Arons & Scharlemann, 1979), in the outer magnetosphere (e.g., Cheng et al., 1986) or outside of the light cylinder through reconnection in the striped wind (e.g., Pétri & Kirk, 2005).

As the most well-studied RPPs, Crab pulsar is considered to be held in SN explosion recorded in 1054 AD and surrounded by a well-known PWN named Crab Nebula. It has the rotation period, surface dipole magnetic field and spin-down luminosity as $P_i \sim 33$ ms, $B_* \sim 10^{13}$ G and $L_{\rm sd} \sim 4.6 \times 10^{38}$ erg s^{-1}, respectively. Despite of the irregular timing behaviors (e.g., Backer, 1970b,a) and the variation in polarization properties (e.g., Słowikowska et al., 2009; Chauvin et al., 2017), one of the unique points of Crab pulsar is that it has almost the same double main peak pulse profile in all energy bands (e.g., Kuiper et al., 2003; Abdo et al., 2010), which implies the overlap of the sites where coherent radio emission and incoherent high energy emission occurs (i.e., around the light cylinder, see Lyubarskii, 1992).

Being represented by Crab pulsar, since the radiation spectrum of synchrotron nebula of RPPs can be perfectly explained by canonical pulsar models, the energy source of RPPs is thought to be rotational energy through magnetic dipole radiation. Their spin-down characteristic age and magnetic field decay time scale are considered to be $\lesssim 100$ Myr and 1-100 Myr, respectively (e.g., Xie & Zhang, 2019); and the surface magnetic field are required to be within the 10^{11}-10^{13} G in order to account for their observed spin-down rate. For pulsars, this range has been broadened in the binary system (e.g., accreting x-ray pulsars, see Harding & Lai, 2006) during the last

half century, from the discovery of milliseconds pulsars that are spun-up by accretion from their binary companion and has much lower surface magnetic field (10^8-10^{10} G, e.g., Backer et al., 1982; Alpar et al., 1982) to the one with much higher period derivatives ($\sim 10^{14}$ G, e.g., Morris et al., 2002; Kaspi et al., 2003b).

1.2.2 Magnetars

Magnetar is a class of NSs that mainly being observed at x-ray and soft γ-ray band with large period derivatives $\dot{P}_i \sim 10^{-12}$-10^{-10} s s^{-1}, and are relatively young given the information provided by x-ray observations of their associated SNRs. In a conventional magnetar model, they generally concentrate around the Galactic plane and are considered to have more massive progenitors (the zero-age main sequence mass here $M_{\rm ZAMS} \gtrsim$ 30-40$M_\odot$) and comparable explosion energy compared to others ($\sim 10^{50}$-10^{51} erg s^{-1}; e.g., Vink & Kuiper, 2006). Despite the expectations that this kind of massive progenitors can evolve into Wolf-Rayet stars and explode as stripped-envelope SNs, the magnetar-forming supernovae (SNe) have not been identified yet (e.g., Enoto et al., 2019).

There mainly exists two types of magnetar: The anomalous x-ray pulsars (AXPs) and soft Gamma-Ray repeaters (SGRs). AXPs are first observed by European X-ray Observatory Satellite (EXOSAT) in the early 1980s as bright x-ray sources with the highest luminosity of $\sim 10^{35}$ erg s^{-1}, relatively narrow range of rotation period $\sim$ 2-12 s and large period derivatives, which initially made them candidates for accreting x-ray pulsars (e.g., Seward et al., 1986). However, there is lack of evidence on detectable companions or accretion disks to support this hypothesis especially considering that no doppler modulation of their x-ray pulses have been identified. On the other hand, the first observation of SGRs can be traced back to 1979, which was detected as a transient sources with repeated soft $\gamma-$ray bursts.

These two subclasses of magnetars are initially considered to be different but turned out to be closely related based on several evidences. Firstly, both of them are discovered with large period derivatives (e.g., $B \sim 10^{14}$-10^{15} G, Vasisht & Gotthelf, 1997) and relatively slow rotation $\sim$ 1-10 s. In addition, they are also identified with recurrent magnetic activities (e.g., sporadic short bursts, see Enoto et al., 2019) and much lower spin-down luminosities ($L_{\rm sd} \sim 10^{32}$-10^{34} erg s^{-1}) compared to the detected x-ray luminosities ($L_{\rm x} \sim 10^{34}$-10^{35} erg s^{-1}). It was until the quiescent x-ray pulsation periods in SGRs with a range of values very similar to those of AXPs and SGR-like bursts from several AXPs are discovered (e.g., Kouveliotou et al., 1998; Kaspi et al., 2003a), and the smaller bursts in this two kinds of sources are found to be similar as well, these two categories are considered to be the same population of isolated NSs that are strongly magnetized ($B \sim 10^{14}$-10^{15} G). The spin-down energy loss of magnetars is insufficient to account for their x-ray luminosity (e.g., Enoto et al., 2017), and their thermal emission in soft x-ray band is typically hotter than RPPs ($kT_{\rm mag} \sim 0.4$ keV) so that the residual heat of conventional cooling curve is insufficient to be their energy source neither. These observational facts suggest the existence of an additional energy source, which has been considered to be the decay of magnetic fields (e.g., Thompson & Duncan, 1993; Woods & Thompson, 2006). Currently, the ultra-strong magnetic field of magnetars is considered to be generated through dynamo in their nascent stage [5], which is greater than the quantum critical field $B_{\rm cr}$ (see the

[5]There are still alternative models for addressing this remarkably large magnetic field: e.g., quark star (e.g., Cea, 2006) and fast rotating massive white dwarf (e.g., Morini et al., 1988).

cyan solid straight lines in Fig. 1.1)

$$\hbar \frac{eB_{\rm cr}}{m_e c^2} = m_e c^2, \tag{1.21}$$

or

$$B_{\rm cr} \equiv \frac{m_e^2 c^3}{\hbar e} = 4.414 \times 10^{13} {\rm G}. \tag{1.22}$$

In this case, the cyclotron energy is comparable to the electron rest mass so that the nonlinear effects becomes important, which introduces additional processes that do not take place in field-free environments (e.g., photon splitting. See Harding & Lai, 2006).

Comparing to the rotation-powered pulsars, such kind of strong magnetic field leads to shorter field decay time scale mainly due to the ambipolar diffusion (e.g., Heyl & Kulkarni, 1998)

$$\tau \cong 10^5 \left(\frac{B_{\rm core}}{10^{15} G} \right)^{-2} {\rm yr}, \tag{1.23}$$

where $B_{\rm core}$ stands for the magnetic field of the NS core. This kind of diffusion sets the dynamical evolution of NS core magnetic field and suggests a yield strain exceeding the crustal strength that is responsible for those small bursts observed both in SGRs and AXPs (e.g., Thompson & Duncan, 1996). In addition, the toroidal component developed under $B_{\rm core} > 10^{15}$ G will be able to cause superflares through reconnection of twisting field lines (e.g., Thompson & Duncan, 2001). The heat transport can also be enhanced under the strong external magnetic field (e.g., Heyl & Kulkarni, 1998), which explains the high temperature of magnetars.

The field decay of magnetars estimates the age of them to be younger than their characteristic-age ($\tau_{\rm c} \sim$ 1-100 kyr), which is broadly consistent with the one suggested by their associated SNRs. This suggests a relatively high formation rate (e.g., ~ 2 century^{-1} for AXPs, see Gill & Heyl, 2007). So far there were only 23 magnetars being confirmed in the Galaxy, Large Magellanic Cloud and Small Magellanic Cloud with respect to $\sim$ 2700 pulsars; where previous studies estimates this percentage to be $\sim$ 1-10% (e.g., Kouveliotou et al., 1994; Heyl & Kulkarni, 1998), and Beniamini et al. (2019) further points out that the fraction of nascent NSs born as magnetars can be constrained through combining their spin-down rates, associated SNRs and magnetic activity as $0.4^{+0.6}_{-0.28}$.

1.2.3 Central Compact Objects

Central Compact Objects (CCOs) are isolated soft x-ray point sources at the center of SNRs that are stable in x-ray and quiet in radio band [6]. The emission is considered to be powered by the residual heat; where the surface luminosity can be shown as

$$L_{\rm CCO} = 4\pi R_*^2 \sigma T_*^4 \sim 1.04 \times 10^{35} {\rm erg\,s^{-1}} \left(\frac{R_*}{10\,{\rm km}} \right)^2 \left(\frac{kT_*}{0.3\,{\rm keV}} \right)^4 \tag{1.24}$$

assuming isotropic radiation. This gives an order-of-magnitude estimates of the NS radius R_* based on the surface temperature T_* obtained from the spectra.

[6] Some of them do exhibit distinctive properties such as pulsating with the period of $P_i \sim 100$ ms in x-ray band with luminosities of $\sim 10^{33}$-10^{34} erg s^{-1}. They have the thermal spectra with temperature ~ 100 eV.

Since CCOs are relatively dim compared to the pulsars and magnetars, only about 10 of them who are close to the earth can be found ($d \sim$ 1-10 kpc, see e.g., Zavlin et al., 2000; Slane et al., 2001; Gotthelf & Halpern, 2009); in addition, the age estimated from the size and the expanding velocity of their associated SNRs is $\sim$ 1-10 kyr, which is much more shorter than their spin-down characteristic age. These two observational facts imply a higher formation rate of CCOs ($\sim$ 1-2 century^{-1}) compared to the one estimated from their spin-down rate.

The surface magnetic fields of three CCOs (i.e., Kes79, Pup-A, G296.5) have been measured to be relatively low as $B_* \sim 10^{10}$-10^{11} G, and their birth periods are close to their current value. They are considered to be relatively young implied by their associated SNRs (i.e., $\sim 10^3$-10^4 yr) and born with low surface magnetic field, which gives their name as "anti-magnetars" (e.g., Halpern & Gotthelf, 2010); although neither associated pulsar wind nebulae (PWNe) nor any counterparts at the other wavelengths have been detected (e.g., Enoto et al., 2019)).

On the other hand, two antipodal hot spots of different temperatures and areas were discovered from RX J0822-4300 in Puppis A (e.g., Gotthelf et al., 2010), which, together with a large pulsed fraction ($\sim$ 64%) from PSR J1852+0040 in Kes79 (e.g., Shabaltas & Lai, 2012), suggest that a stronger magnetic field other than dipole may exist in CCOs. In the case of isolated NS 1E 1207.4-5209 associated with SNR GG296.5+10.0, the absorption at 0.7, 1.4 and 2.1 keV in the x-ray energy spectrum also imply the existence of multi-polar magnetic fields since this phenomenon can basically be explained by the atomic transitions under strong magnetic fields (e.g., Hailey & Mori, 2002; Mori et al., 2013). In addition, there exist candidates that either has CCO-like properties but locates near young radio pulsars in the P_i-$\dot{P}_i$ phase diagram (e.g., 1RXS J141256.0+792204, or dubbed 'Calvera' with $P = 59$ ms, $L_{\rm sd} = 6 \times 10^{35}$ erg s^{-1} and $\tau_{\rm c} = 3 \times 10^5$ yr, see Rutledge et al., 2008; Shevchuk et al., 2009) or has magnetar-like activities (e.g., 1E 161348-5055 at the centre of SNR RCW103, see Tuohy & Garmire, 1980).

In order to connect these observations into one cohesive picture with a physical explanation, one leading theory is that CCOs may born with relatively strong magnetic field $B_* \sim 10^{12}$-10^{13} G buried under the prompt supernova fallback accretion, which will re-emerge after $\sim$ 1-10 kyr to evolve into RPPs/magnetars-like objects (e.g., Muslimov & Page, 1995).

1.3 Important processes to determine the magnetic field strength of NSs

In summary, one of the key parameters among RPPs, magnetars and CCOs is the magnetic field strength: the strengths of the dipole field are estimated to be $B_{\rm d} \sim 10^{12\text{-}13}$ G for rotation-powered pulsars (e.g., Enoto et al., 2019), $B_{\rm d} \gtrsim 10^{14}$ G for magnetars (e.g., Kaspi, 2007; Kaspi & Beloborodov, 2017), and $B_{\rm d} \lesssim 10^{11}$ G for CCOs (e.g., Ho & Heinke, 2009; Pavlov & Luna, 2009), respectively. The origin of this diversity is still unsettled.

By the end of the stellar evolution, metals form in fusion stages after the hydrogen is depleted in the stellar core, and eventually results in an nickel-iron core enshrouded by a shell of burning material (e.g., a mixture of silicon, sulfur and etc.). Since iron absorb energy to enter the next stage of fusion instead of providing energy, the core with the mass near the Chandrasekhar limit $M \sim 1.4\,M_\odot$ forms into an energy sink and begins to collapse under the gravity, which produces high energy photons by significantly raising the temperature in the inner core. These

γ-ray photons breaks the heavy nucleus through photo-disintegration. The protons are forced to capture electrons to form neutrons

$$p^+ + e^- \rightarrow n + \nu_e \tag{1.25}$$

as called the inverse-β decay, with a vast amount of neutrinos trapped when core density $\rho_{\rm core} \gtrsim 10^{12}$ g cm^{-3}, since their diffusion time scale due to coherent conservative scattering on nuclei is essentially longer than the collapsing time scale (e.g., Bethe, 1990). This kind of neutrino trapping typically happens at ~ 0.1 s, and the core collapse then proceeds homogeneously (e.g., Goldreich & Weber, 1980) until reaching the nuclear density; since the gravity is extremely difficult to further compress the core under the nuclear force, the innermost collapsing core decelerates and eventually bounces, which drives an outgoing shock to the infalling outer core at ~ 0.11 s. Neutrinos will be released when the shock propagates, and is considered to be important for reviving the shock after it stagnates and leads to a successful supernova explosion at ~ 0.2 s. Until the explosion sets in, a compact remnant, which is rapidly fed by the infalling stellar material, will form at the center of the collapsing star after the core bounce. It evolves into an NS if the progenitor mass $M \lesssim 25 M_\odot$ (e.g., Janka et al., 2007).

The nascent NS is born to be proton-rich with containing a huge amounts of degenerate electrons and trapped neutrinos with shorter mean free path comparing to the NS radius. Those neutrinos diffuse out and cool the hot interior region of proto-NS mainly through converting their degeneracy energy to thermal energy of the stellar medium (e.g., Burrows, 1990) in a fraction of one second, which will lead to the early post-explosion wind dominated by neutrino. The neutrino-driven wind catches up to the tail of the supernova ejecta and further pushes it outward, in which a nascent magnetosphere will be formed inside the bubble produced by it. However a tail part of the ejecta that is marginally bound falls back to the newborn NS either when the neutrino luminosity from the NS significantly decreases in ~ 10 s (e.g., Burrows, 1988; Ugliano et al., 2012) or the supernova shock clashes into the thick outer envelope (Chevalier, 1989).

The magnetic field strength of a isolated NS born in the CCSN explosion should be determined as a consequence of several processes, which can be basically categorized into

- fossil scenario where the magnetic field of the progenitor core of central NS can be amplified by the flux-freezing contraction (since their radius generally shrinks from $\sim 10^3$-10^4 km to ~ 10 km, e.g., Woltjer, 1964)

$$M R^2 \Omega = \text{const.}, \tag{1.26}$$

$$B R^2 = \text{const.}, \tag{1.27}$$

  with the M, R, Ω and B to be the mass, radius, angular frequency and magnetic field of the core; and

- dynamo scenario that generally considers the effects of turbulence. It mainly includes the α-Ω dynamo (e.g., Duncan & Thompson, 1992; Thompson & Duncan, 1993); the magnetorotational instability (e.g., Akiyama et al., 2003; Thompson et al., 2005) occurring in the proto-NS, and/or stationary accretion shock instability (SASI) of the post-bounce core-collapse supernova environment (e.g., Endeve et al., 2012).

On the other hand, the magnetic field usually decay via the combination of the ambipolar diffusion, the Hall drift, and the Ohmic diffusion (Goldreich & Reisenegger, 1992); and the supernova fallback was also considered to be relevant for NS magnetic field strength, especially for explaining the apparently weak magnetic field of the CCOs (e.g., Muslimov & Page, 1995; Torres-Forné et al., 2016).

The fallback matter can be characterized by two physical quantities: the total fallback mass $M_{\rm fb}$ and fallback timescale $t_{\rm fb}$, which shall be determined by the complex supernova explosion dynamics and the core structure of the progenitor star (e.g., see Fig. 1.3 for reference). It will proceed down to the near NS surface region if there is no repulsing force, and the magnetosphere of the newborn neutron star can be strongly disturbed: the magnetic field lines that are initially closed will be forced to open under such an accretion and thus enhance the spin-down torque of the NS (e.g., Parfrey et al., 2016, see Fig. 1.4 for reference). In the extreme case, the magnetic field can be buried under the non-convective crust with the fallback matter (e.g., Torres-Forné et al., 2016, see Fig. 1.5 for reference).

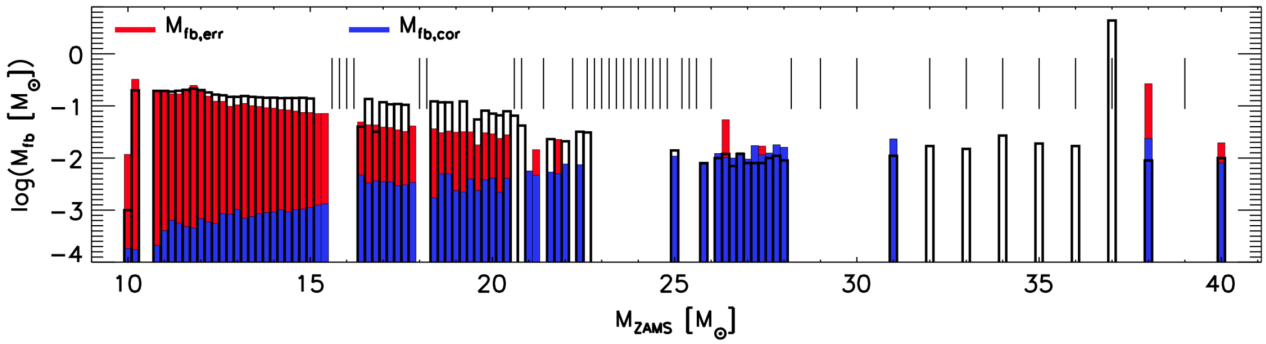

Figure 1.3: Repost from the fig.1 in Ugliano et al. (2012): Total fallback mass for the progenitors studied by Ugliano et al. (2012). The white histogram bars show the results of Ugliano et al. (2012), the red bars display the simulation results given by Ertl et al. (2016a) with modeling improvements in various aspects and incorrect fallback estimate of their Equation (1); the blue histogram bars show the cases computed by Ertl et al. (2016a) with the correct fallback determination according to their Equation (2). The vertical lines in the upper part indicate non-exploding cases obtained by Ertl et al. (2016a).

On the other hand, the electromagnetic waves associated with the angular momentum loss of the central NS is considered to be efficient for accelerating the charged particles being ejected to the magnetosphere to relativistic energy scale (e.g., Pacini, 1967; Ostriker & Gunn, 1969). Such kind of relativistic outflow powered by extracting rotation energy from the central NS through unipolar induction becomes dominant after neutrino luminosity significantly decreases, where its luminosity can be approximated by the canonical pulsar model as

$$L_{\rm d} = \frac{{B_*}^2 {\Omega_{\rm i}}^4 R_*^6}{4c^3} \left(1+\sin\chi^2\right) \sim 4.3\times10^{41}{\rm ergs}^{-1} \left(1+\sin\chi^2\right) {B_{*,13}}^2 P_{\rm i,-2}^{-4} \tag{1.28}$$

with χ being the inclination angle between rotation and dipole axes; an oblique rotator is commonly found before the system reaches equilibrium through dissipating energy by stresses or magneto-hydrodynamic waves at the NS surface (e.g., Tchekhovskoy et al., 2013). As pointed out in Sec. 1.2, since the surface magnetic field B_* and rotation period P_i of newborn NS range from $[10^{10}, 10^{16}]$ G and $[1, 10^4]$ ms, respectively; the dynamical range of spin-down luminosity is

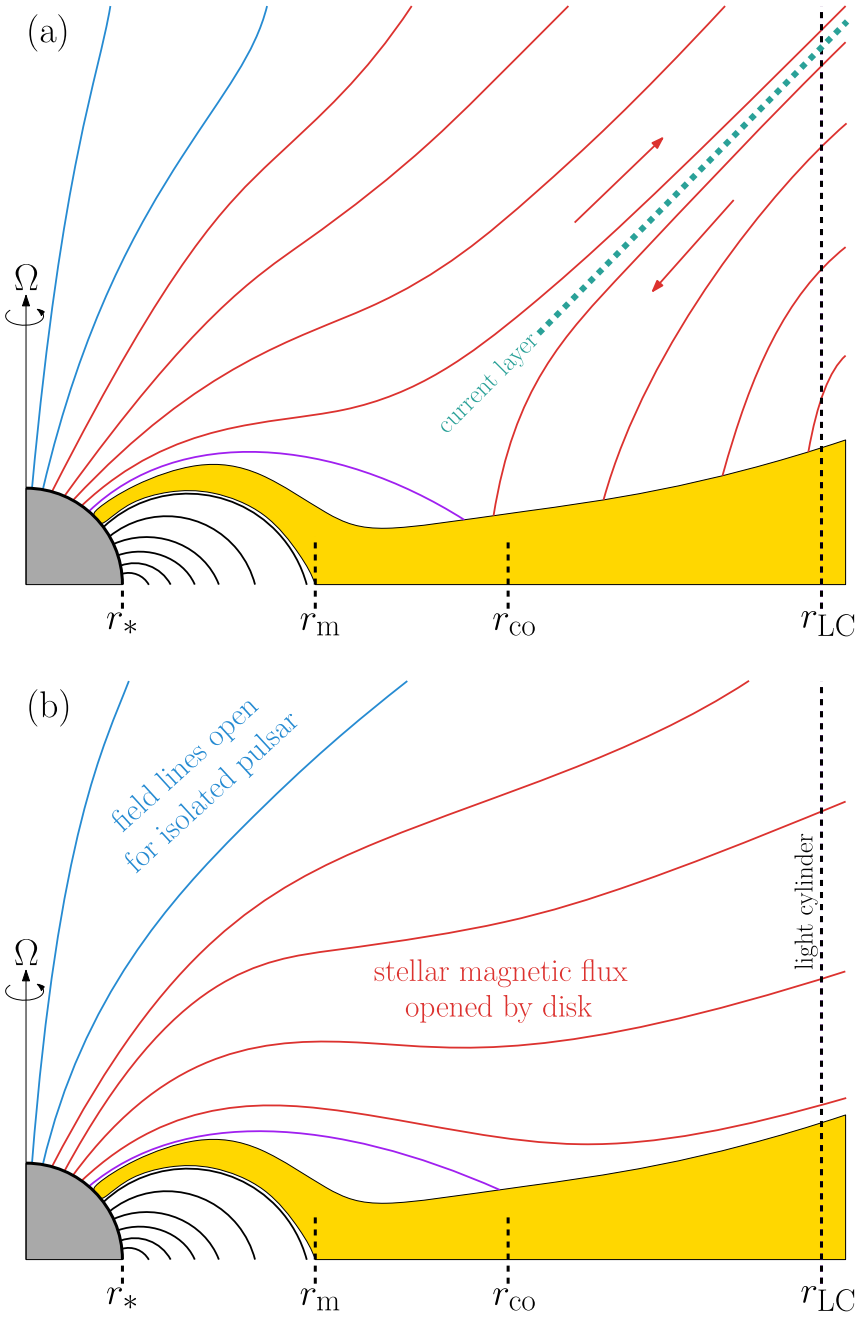

Figure 1.4: Repost from the fig.1 in Parfrey et al. (2016): Schematic accretion flow and magnetic field geometry for their proposed accretion model, which shows the disk outside r_m (the inner boundary of the Keplerian disk, or the magnetospheric radius) and the accretion funnel inside r_m (gold region). Most stellar flux that would otherwise couple to the disk is forced to open (red lines) except for a small amount of flux trapped near the co-rotation radius (see the purple lines). Open field lines in the magnetosphere of an isolated pulsar with angular frequency Ω are indicated in blue lines. Figure (a) shows the stellar field lines that have opened and form a current layer (see the cyan dashed line), where the red arrows indicate the poloidal direction of the field on either side of the layer. Figure (b) shows the relaxed state, where parts of the open stellar field lines that are rooted in the disk have been pushed beyond the light cylinder.

Figure 1.5: Repost from the fig.5 in Torres-Forné et al. (2016): fallback accretion bury the magnetic field of NS when $\dot{M} \gtrsim 10^{-5} M_\odot\,\mathrm{s}^{-1}\,(B_*/10^{13}\mathrm{G})^{3/2}$ (see the left panel) with B_* being the surface magnetic field strength of NS. The upper-most panel stands for the initial state, the left column shows the expected evolution for NS with magnetic field $B \lesssim 10^{13}$ G; while the right column corresponds to the other end $B \gtrsim 10^{13}$ G. In which they assume the mass accretion rate $\dot{M} = 10^{-5}\ M_\odot\,\mathrm{s}^{-1}$.

relatively as broadly as the mass accretion rate of supernova fallback. We consider the interaction between supernova fallback accretion and outflow from the newborn NS magnetosphere to be responsible for three different types of magnetospheric structure, which may account for the trifurcation of NSs. In this scenario, outflow from the nascent magnetosphere tends to repulse the falling back matter: if it repels the fallback accretion, a pulsar with clean magnetosphere may form; otherwise the magnetosphere will be disturbed or even buried, which lead to the formation of magnetars with synthesized multipole magnetic field and CCOs with apparently weak magnetic field (e.g., Shigeyama & Kashiyama, 2018).

In order to derive the trifurcation point, Shigeyama & Kashiyama (2018) constructed a self-similar solution without scale dependence for a spherically symmetric fallback accretion confronting with a relativistic pulsar wind, which is a one-parameter family of the out- to inflow luminosity ratio. However there is still a long way to go in exploring the effect of other physical quantities (e.g., where the in- and outflows collides, the Lorentz factor of the outflow and so on) in numerical simulation. In this thesis, we follow the system and its self-similar solution given by Shigeyama & Kashiyama (2018), and perform a suit of relativistic hydrodynamic simulations to clarify the condition for the fallback matter invading down to the NS magnetosphere and how it is affected by the parameter space we consider.

This thesis is organized as follows. We describe the problem setting in Sec. 2, and show the results of the numerical simulation in Sec. 3. We consider the implications of the results for the diversity in young NSs in Sec. 4. Sec. 5 is devoted to the summary, discussion and future perspectives. The analytical model we built for explaining the simulation results is shown in App. A, and the Rayleigh-Taylor instability analysis towards the shock interface existed in the system is performed in App. B. We use the convention of $Q_x = Q/10^x$ in cgs units unless otherwise noted.

Chapter 2

Methods

In this thesis, we mainly consider the mass accretion that is induced when the neutrino luminosity from the NS significantly decreases (e.g., Ugliano et al., 2012); while the rotation-powered relativistic wind becomes the dominant outflow component. In order to find the critical condition for the fallback matter to reach near the NS surface, we numerically investigate the dynamics of the supernova fallback accretion confronting with the relativistic wind. The initial condition (Sec. 2.1) and technical details (e.g., boundary conditions in Sec. 2.2, governing equations and numerical scheme in Sec. 2.3) of our simulation will be shown as follows.

2.1 Initial condition

As shown in Fig. 2.1, we consider a fallback matter with mass accretion rate $\dot{M}_{\rm fb}$ to be encountered with a relativistic outflow with luminosity of L and terminal Lorentz factor of Γ_∞ at an encounter radius of $r = r_{\rm enc}$. The system is characterized by three dimensionless parameters (ζ, $\mathcal{R}_{\rm enc}$, Γ_∞), where

$$\zeta = \frac{L}{\dot{M}_{\rm fb,ini}c^2} \tag{2.1}$$

is a dimensionless parameter being the ratio between the outflow luminosity and the initial fallback accretion rate $\dot{M}_{\rm fb,ini}$, and

$$\mathcal{R}_{\rm enc} = \frac{r_{\rm enc}}{r_{\rm Sch}} \tag{2.2}$$

with

$$r_{\rm Sch} = \frac{2GM_*}{c^2} \tag{2.3}$$

to be the Schwarzschild radius of the central NS with mass M_*. In this paper, we consider a spherically symmetric one-dimensional system in order to explore a wide range of these parameters.

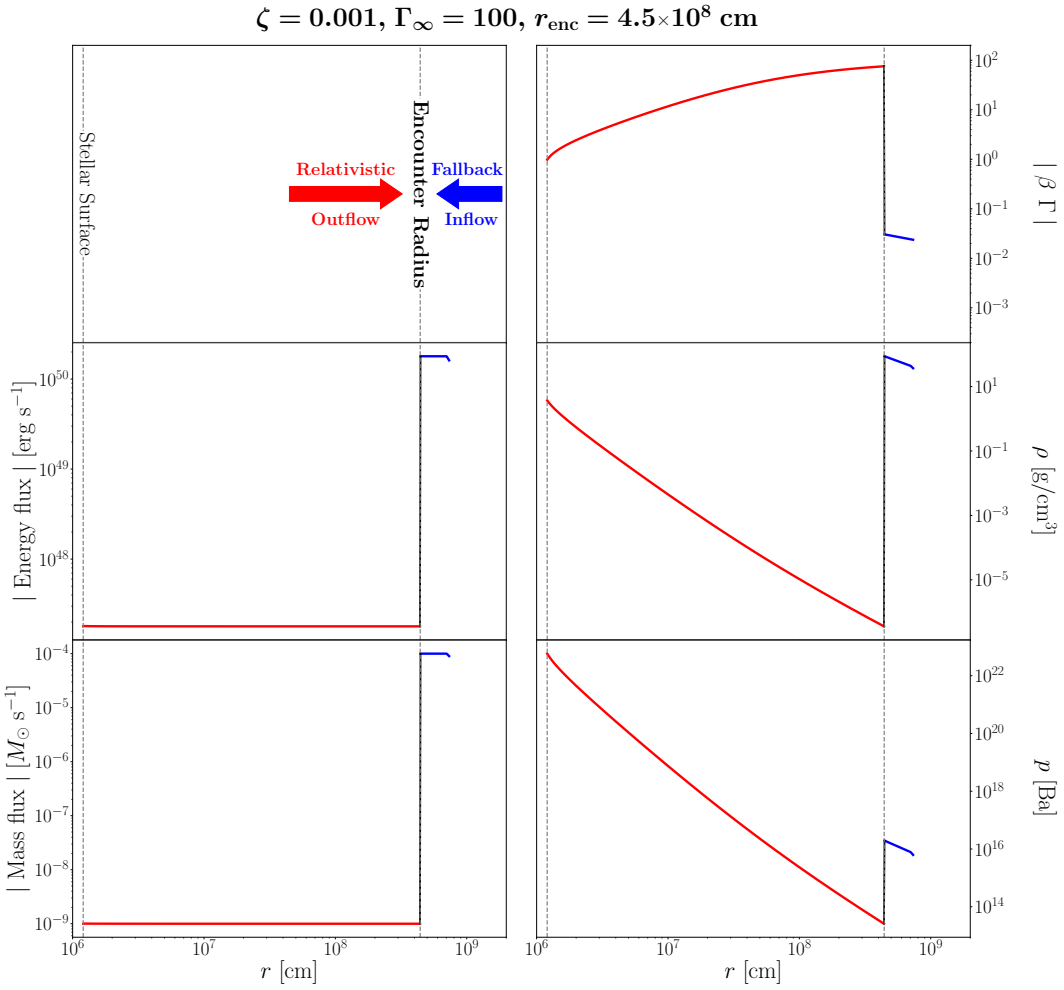

Figure 2.1: An example of initial condition of our simulation. A relativistic outflow with a terminal Lorentz factor $\Gamma_\infty = 100$ collides with a fallback matter at the encounter radius $r_{\rm enc} = 4.5 \times 10^8\,{\rm cm}$. The dimensionless out- to inflow energy flux ratio (Eq. 2.1) is $\zeta = 0.001$. We take the absolute value of the velocity $\beta\Gamma$, energy and mass fluxes, while the sign should be positive in the outflow region and negative in the inflow region.

2.1.1 Fallback accretion

The fallback accretion typically sets in at $t_{\rm fb} \sim 10\,{\rm s}$ after the supernova explosion and the total fallback mass ranges over $M_{\rm fb} \sim 10^{-(2\text{-}4)}\,M_\odot$, depending on the core structure of the progenitor (e.g., Ugliano et al., 2012; Ertl et al., 2016b, see Sec. 1.3 and Fig. 1.3 for reference as well), which leads to the fallback accretion rate of $\dot{M}_{\rm fb} \sim 10^{-3} - 10^{-6}\,M_\odot\,{\rm s}^{-1}$.

Here we assume that the fallback accretion rate evolves with times as

$$\dot{M}_{\rm fb} = \dot{M}_{\rm fb,ini} \times \begin{cases} 1 & t \le t_{\rm fb} \\ (t/t_{\rm fb})^{-l} & t > t_{\rm fb} \end{cases}, \tag{2.4}$$

where

$$\dot{M}_{\rm fb,ini} = \frac{l-1}{l}\frac{M_{\rm fb}}{t_{\rm fb}} \sim 1 \times 10^{-5}\,M_\odot\,{\rm s}^{-1} \left(\frac{l-1}{l}\right) M_{\rm fb,-4}{t_{\rm fb,1}}^{-1} \tag{2.5}$$

with $l > 1$ to ensure the total fallback mass to be $M_{\rm fb}$. Since that the fallback matter we consider here is originated from the tail part of the supernova ejecta that were outflowing but marginally bounded to the NS, it is set to have the free-fall velocity at radius r

$$v_{\rm fb}(r) = -\sqrt{\frac{2GM_*}{r}}, \tag{2.6}$$

where $M_* = 1.4\,M_\odot$ is the neutron star mass; and the fiducial value of time dependence of mass accretion rate l is set to be 5/3 in Eq.(2.4), which has been predicted by Chevalier (1989) under this circumstance and was confirmed by numerical simulations of supernova explosion as well (e.g., Janka et al., 2021). We here consider unshocked fallback matter to be sufficiently cold so that its density profile can be determined with the inward mass flux (see Eq. 2.4) by assuming that it is in a steady state as

$$\rho_{\rm fb}(r) = \frac{\dot{M}_{\rm fb}}{4\pi r^2\,|v_{\rm fb}\,(r)|}, \tag{2.7}$$

and the pressure profile can be thus obtained through adiabatic equation of state with adiabatic index $\gamma = 4/3$ as

$$p_{\rm fb}(r) = k_{\rm fb}\rho_{\rm fb}(r)^\gamma. \tag{2.8}$$

Where the coefficient $k_{\rm fb}$ is given by fixing the sound velocity at the outer edge of the infalling region as $c_{\rm s} \sim 10^{-3}c$.

2.1.2 Relativistic wind

As the dominant component of post supernova explosion outflow after the neutrino-wind ceases, the wind powered by the spindown luminosity of young NS (e.g., Pacini, 1967; Ostriker & Gunn, 1969) is considered here. It is being modeled as a relativistic hydrodynamic wind with a terminal Lorentz factor Γ_∞ (which mainly depends on the baryon loading and magnetization of the embryonic magnetosphere) and luminosity L to study its impact on the fallback accretion dynamics parametrically. In this case, the wind profile can be obtained by solving the following

equations for a given set of (L, Γ_∞);

$$4\pi r^2 \beta_{\rm w} {\Gamma_{\rm w}}^2 \rho_{\rm w} h_{\rm w} c^3 = L, \tag{2.9}$$

$$4\pi \Gamma_{\rm w} \beta_{\rm w} \rho_{\rm w} r^2 c^3 = \frac{L}{\Gamma_\infty}, \tag{2.10}$$

where

$$\Gamma_{\rm w} = \frac{1}{\sqrt{1 - {\beta_{\rm w}}^2}} \tag{2.11}$$

and

$$h_{\rm w} = 1 + \frac{\gamma}{(\gamma - 1)} \times \frac{p_{\rm w}}{\rho_{\rm w} c^2} \tag{2.12}$$

are the Lorentz factor and the specific enthalpy with $\beta_{\rm w} = v_{\rm r}/c$ and $\rho_{\rm w}$ being the dimensionless velocity and proper mass density; Pressure profile in the outflow region can be determined by adiabatic equation of state with $\gamma = 4/3$ being the adiabatic index:

$$p_{\rm w} = k_{\rm w} {\rho_{\rm w}}^{\gamma}. \tag{2.13}$$

Here we assume that the matter is ejected with trans-relativistic velocity $\beta_{\rm w}(R_*) = 0.7$ [1]. The constant $k_{\rm w}$ is set to ensure the Lorentz factor of the wind at infinity to be Γ_∞. Note that the wind luminosity L is constant in the following calculations, since the spindown timescale $t_{\rm sd}$ is typically much longer than the dynamical timescale we are interested in (see Eq.(4.4)).

2.1.3 The encounter radius

The encounter radius $r_{\rm enc}$ is basically where the outflow and fallback matter encounters and should corresponds to the fallback radius $r_{\rm fb}$ that the fallback matter starts to fall back to the central NS after the neutrino-driven wind ceases. Since the fallback timescale should be roughly one free-fall timescale from $r_{\rm fb}$, it shall be given as

$$r_{\rm fb} = (G M_* {t_{\rm fb}}^2)^{1/3} \sim 2.7 \times 10^9 \,{\rm cm}\, {t_{\rm fb,1}}^{2/3}. \tag{2.14}$$

Considering the case of a relativistic wind, in which the propagation timescale of the wind from the NS surface to the fallback radius is negligible compared with the fallback timescale, the fallback matter and the relativistic wind should practically encounter at [2]

$$r_{\rm enc} \approx r_{\rm fb} \sim 2.7 \times 10^9 \,{\rm cm}\, {t_{\rm fb,1}}^{2/3}, \tag{2.15}$$

which is in principle supposed to be derived by the complex supernova explosion dynamics and sensitive to the core structure of the progenitor star. However here in one-dimensional spherical hydrodynamics study, we define it as a model parameter of our simulation.

[1] This treatment enhances the numerical stability; in the case of setting a relativistic velocity at the inner boundary, a numerical instability occurs when the reverse shock approaches the boundary.

[2] Note that the encounter radius is typically much larger than the light cylinder radius (see Eq.(1.13)).

2.2 Boundary condition

The inner boundary in our simulations is fixed to be at $R_* = 12\,\mathrm{km}$, while the outer boundary $r_{\rm out}$ is set to be sufficiently larger than the encounter radius of the in- and outflows. For a given fallback rate $\dot{M}_{\rm fb}$ shown in Eq.(2.4), we set the velocity, density and pressure profile at the outer boundary $r_{\rm out}$ following Eq.(2.16), (2.17) and (2.18), respectively.

$$v_{\rm fb}(r_{\rm out}) = -\sqrt{\frac{2GM_*}{r_{\rm out}}}, \tag{2.16}$$

$$\rho_{\rm fb}(r_{\rm out}) = \frac{\dot{M}_{\rm fb}}{4\pi r_{\rm out}^2 \left|v_{\rm fb}\left(r_{\rm out}\right)\right|}, \tag{2.17}$$

$$p_{\rm fb}(r_{\rm out}) = k_{\rm fb}\rho_{\rm fb}(r_{\rm out})^{\gamma}. \tag{2.18}$$

while the corresponding physical profiles in the ghost cell can be determined as follows:

$$v_{\rm r}{}^{iu+i,j,k} = v_{\rm r}{}^{iu,j,k}\left(\frac{r_{iu}}{r_{iu+i}}\right)^{\frac{1}{2}}, \tag{2.19}$$

$$\rho^{iu+i,j,k} = \rho^{iu,j,k}\left(\frac{r_{iu}}{r_{iu+i}}\right)^{\frac{3}{2}(l+1)}, \tag{2.20}$$

$$p^{iu+i,j,k} = p^{iu,j,k}\left(\frac{\rho^{iu+i,j,k}}{\rho^{iu,j,k}}\right)^{\gamma} \tag{2.21}$$

with i loops from 1 to the number of ghost cells $N_{\rm ngh}$, and iu stands for the outer-most cell else than the ghost cells at the outer boundary. On the other hand, for a given outflow luminosity L, the density and pressure at the inner boundary (i.e. NS radius R_*) are determined from Eq.(2.9), (2.10) as

$$v(R_*) = \beta_{\rm w}(R_*) = 0.7c, \tag{2.22}$$

$$\rho(R_*) = \rho_{\rm w}(R_*) = \frac{L}{4\pi\Gamma_\infty\Gamma_{\rm w}(R_*)\beta_{\rm w}(R_*){R_*}^2c^3}, \tag{2.23}$$

$$p(R_*) = p_{\rm w}(R_*) = \left[\left(\frac{\Gamma_\infty}{\Gamma_{\rm w}(R_*)} - 1\right)\frac{\gamma-1}{\gamma}\right]\rho_{\rm w}(R_*)c^2. \tag{2.24}$$

with fixing corresponding physical profiles in the ghost cells:

$$v_{\rm r}{}^{il-i,j,k} = \beta_{\rm w}(R_*), \tag{2.25}$$

$$\rho^{il-i,j,k} = \rho_{\rm w}(R_*), \tag{2.26}$$

$$p^{il-i,j,k} = p_{\rm w}(R_*), \tag{2.27}$$

where i loops from 1 to the number of ghost cells $N_{\rm ngh}$, and il stands for the inner most cell else than the ghost cells at the inner boundary.

2.3 Numerical simulation

Conservation laws under special relativity can be expressed as follows:

$$\left(\rho u^{\mu}\right)_{,\mu} = 0, \tag{2.28}$$

$$T^{\mu\nu}{}_{,\nu} = F^{\mu}, \tag{2.29}$$

where F^{μ} stands for source term that can be specified regarding physical settings, u^{μ} and $T^{\mu\nu}$ represents the velocity four-vector and stress-momentum tensor, respectively:

$$u^{\mu} = \left(1, \Gamma v^{i}\right), \Gamma = \frac{1}{\sqrt{1 - \left\|v^{i}\right\|^{2}}}, \tag{2.30}$$

with v_i to be 3-velocity, and

$$T^{\mu\nu} = \rho h u^{\mu} u^{\nu} + p\eta^{\mu\nu}, \tag{2.31}$$

$$\eta^{\mu\nu} = \begin{pmatrix} -1 & 0 & 0 & 0 \\ 0 & 1 & 0 & 0 \\ 0 & 0 & 1 & 0 \\ 0 & 0 & 0 & 1 \end{pmatrix}, \tag{2.32}$$

where ρ is proper mass density, p is gas pressure, and velocity of light c is taken as 1 here. h stands for special enthalpy and can be expressed as:

$$h = 1 + \epsilon + \frac{p}{\rho}, \tag{2.33}$$

where ϵ is specific internal energy, and can be fixed by the equation of state (EoS). Here we assume an adiabatic EoS with an adiabatic index of $\gamma = 4/3$, in which h can be specified as

$$h = 1 + \frac{p}{(\gamma - 1)\rho} + \frac{p}{\rho}. \tag{2.34}$$

Based on the initial conditions and boundary conditions given in the previous section, if we define the the mass, momentum, and energy densities as

$$D = \Gamma\rho, \tag{2.35}$$

$$S = \Gamma^{2}\rho h\beta \tag{2.36}$$

and

$$E = \Gamma^{2}\rho h - p \tag{2.37}$$

with $\beta = v^{r}$ being the radial velocity, the time evolution of the shock structure under the spherical symmetry can obtained by numerically solving one-dimensional relativistic hydrodynamic equations with a gravity source term derived from Eq. (2.28) and Eq. (2.29) as follows;

$$\frac{\partial D}{\partial t} + \frac{1}{r^{2}}\frac{\partial}{\partial r}\left(D\beta r^{2}\right) = 0, \tag{2.38}$$

$$\frac{\partial S}{\partial t} + \frac{1}{r^2}\frac{\partial (r^2 S\beta)}{\partial r} + \frac{\partial p}{\partial r} = -\frac{GM_*}{r^2}D, \tag{2.39}$$

$$\frac{\partial E}{\partial t} + \frac{1}{r^2}\frac{\partial}{\partial r}\left(r^2 S\right) = -\frac{GM_*}{r^2}S. \tag{2.40}$$

Here we use Athena++ code (Stone et al., 2020) for the numerical integration with employing the Harten-Lax-van Leer-Contact (HLLC) Riemann solver (Mignone & Bodo, 2005) and the second-order piecewise linear reconstruction method (PLM) with van Leer slope limiter (Van Leer, 1974). The time integration is carried out by the second order Runge-Kutta method with a Courant-Friedrich-Lewy number of 0.1. The computational domain is resolved with the mesh number of 1024 with a non-uniform mesh, where the fiducial value of the grid size ratio $\Delta r(i+1)/\Delta r(i)$ is 1.009 (i.e., the radial grid size is positively correlated to the radius), and the results convergence regarding the spatial resolution has been confirmed. Given the mesh spacing, we numerically set the initial condition with the cubic B spline (Burkardt, 2020) based on the wind profile obtained in the outflow region (see Eqs. (2.9) and (2.10)).

The parameter space shown in Table 2.1 will be investigated in this thesis (~ 200 cases), where four different encounter radii ($r_{\rm enc} = 4.5\times10^7$, 1.8×10^8, 4.5×10^8, 1.8×10^9 cm) and three different terminal Lorentz factors ($\Gamma_\infty = 6, 10$ and 100) are considered. For a given combination of $(r_{\rm enc}, \Gamma_\infty)$, we try a few 10 different ζ values in the range of $[10^{-5} : 10]$ through fixing the fallback accretion rate at $\dot{M}_{\rm fb,i} = 10^{-4}\,M_\odot\,{\rm s}^{-1}$ and varying the wind luminosity L [3].

parameter	notation	range	unit
out- to inflow luminosity ratio	ζ	$[10^{-5} : 10]$	
outflow Lorentz factor at infinity	Γ_∞	$[2 : 100]$	
normalized encounter radius	$\mathcal{R}_{\rm enc}$	$[100 : 10000]$	

Table 2.1: Run parameters

[3]We have confirmed that the same (ζ, $\mathcal{R}_{\rm enc}$, Γ_∞) but different (L,$\dot{M}_{\rm fb,i}$) cases give the same minimum fallback radii, which coincides with the Bukcingham Pi theorem that states ALL theories must be able to be written in terms of dimensionless parameters.

Chapter 3

Results

Here in this chapter, we will briefly show the results given the numerical settings shown in Sec. 2 and parameter space we considered in Tab. 2.1.

First of all, when the fallback inflow collides with the outflow, several discontinuities develop (see Fig. 3.1), which evolve differently depending on the system's outflow to inflow luminosity ratio ζ (see Fig. 3.2 and Fig. 3.3). A forward shock separates the shocked and unshocked fallback matter (see the blue vertical dotted line in Fig. 3.1); a reverse shock separates the shocked and unshocked winds (see the red vertical dotted line in Fig. 3.1); and a contact surface separates the shocked fallback matter and the shocked wind (see the green vertical dotted line in Fig. 3, where the gas density reaches its maximum value). In this physical picture, the bulk position of the fallback matter $r_{\rm fb}$, namely the fallback radius, can be regarded as the position of the contact surface. There is also an interface where the flow velocity changes sign, i.e. the instantaneous in- and outflow boundary, in addition to the three discontinuities (see the yellow vertical dotted line in Fig. 3.1); when $r_{\rm fb}$ is decreasing, it resides between the contact surface and the reverse shock, otherwise it appears between the contact surface and the forward shock.

Figs. 3.2 summarizes the dynamical evolution of the velocity (top row), density (middle row) and pressure profiles (bottom row) for the fallback-outflow systems encountering at $r_{\rm enc} = 4.5 \times 10^8$ cm with the same wind Lorentz factor of $\Gamma_\infty = 100$ but different energy flux ratios $\zeta = 0.00035$ (left column), 0.001 (central column) and 0.03 (right column); in which the time evolution of the shock structures (e.g., the forward shock, the reverse shock, and the contact surface) can be extracted to Fig. 3.3: we mark the encounter radii, the minimum reverse shock radii $r_{\rm rs,min}$ and the minimum fallback radii $r_{\rm fb,min}$ as the solid, dash and dotted-dash horizontal lines so that the entire shocked regions will be red shaded. One relevant time scale $t = t_{\rm fb}$ here is indicated by the vertical dotted line.

What we can learn from Figs. 3.2 and 3.3 is that there generally exist three categories of shock structure evolution regarding the energy flux ratio ζ. In the relatively large ζ limit, the fallback radius $r_{\rm fb}$ monotonically increases (see the right panels) with $r_{\rm fb,min} = r_{\rm enc}$ by definition [1]; while at the other end, the fallback matter starts from the encounter radius $r = r_{\rm enc}$ and reaches down to the NS surface in about one free-fall time ($t \sim 600$ ms) with $r_{\rm rs,min} = r_{\rm fb,min} = R_*$, i.e., the shocked region monotonically contracts (see left panels). As for the cases in between, the shocked region initially contracts to the minimum radius and expands afterward, in which

[1] We note that even in this case the reverse shock radius can decrease for a while after the encounter.

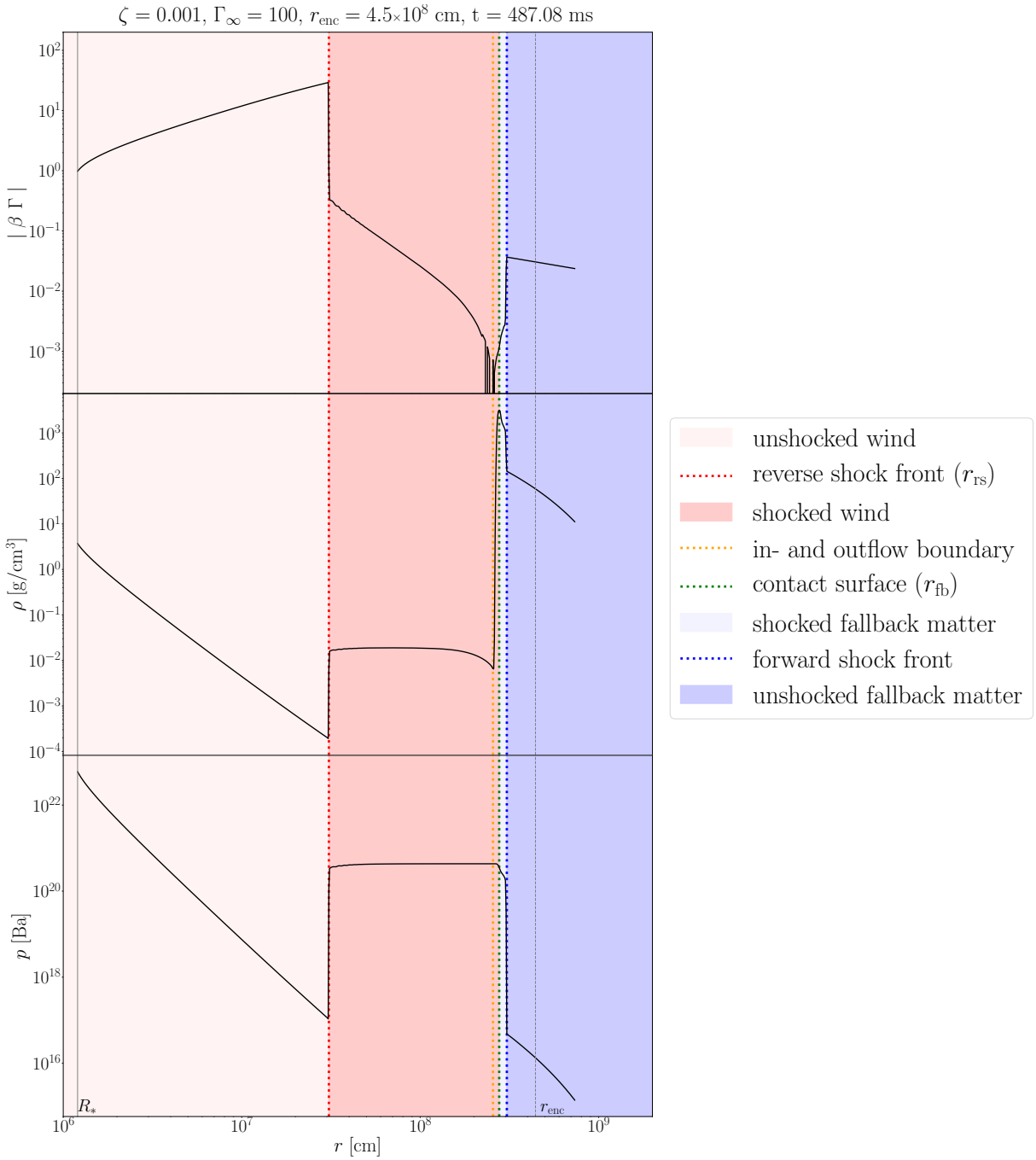

Figure 3.1: Shock structure developed when relativistic outflow with a terminal Lorentz factor of $\Gamma_\infty = 100$ encounters with the fallback matter at a radius of $r_{\rm enc} = 4.5 \times 10^8$ cm (see the dashed line) with energy flux ratio $\zeta = 0.001$. The top, middle, and bottom panels show the velocity, density, and pressure profiles at time $t = 487.08$ ms, respectively. The discontinuities and the stellar surface are marked by the vertical dotted and solid lines, respectively.

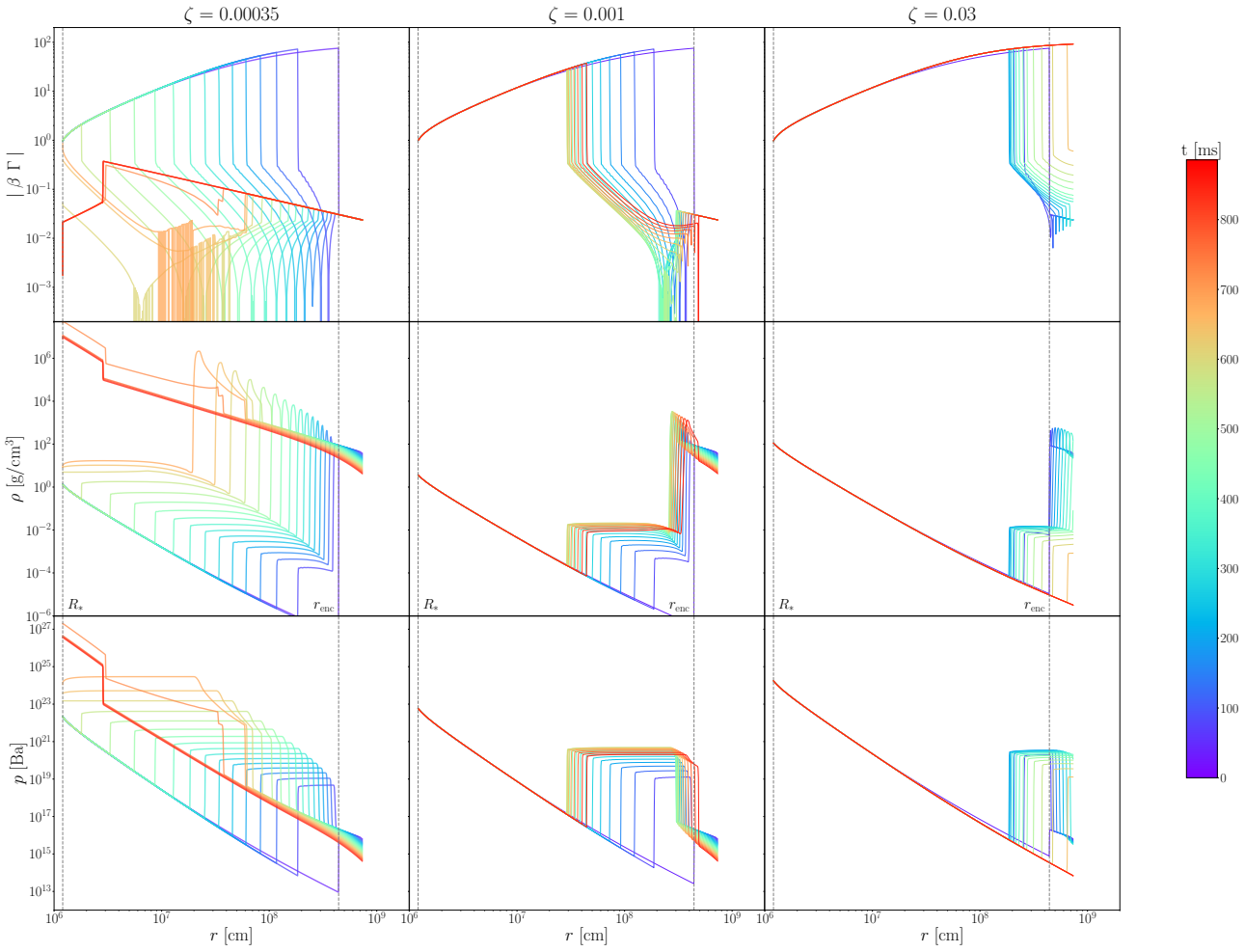

Figure 3.2: Time evolution of the hydrodynamic structure after a relativistic outflow with a terminal Lorentz factor of $\Gamma_\infty = 100$ collides with a fallback matter at a radius of $r_{\rm enc} = 4.5\times10^8$ cm (see the vertical dashed lines) for $0 < t < 885.6$ ms. The cases with three different out- and inflow luminosity ratios are shown : $\zeta = 0.00035$ (left), 0.001 (center) and 0.03 (right). The velocity, density and pressure profiles are shown in top, middle and bottom panels, respectively.

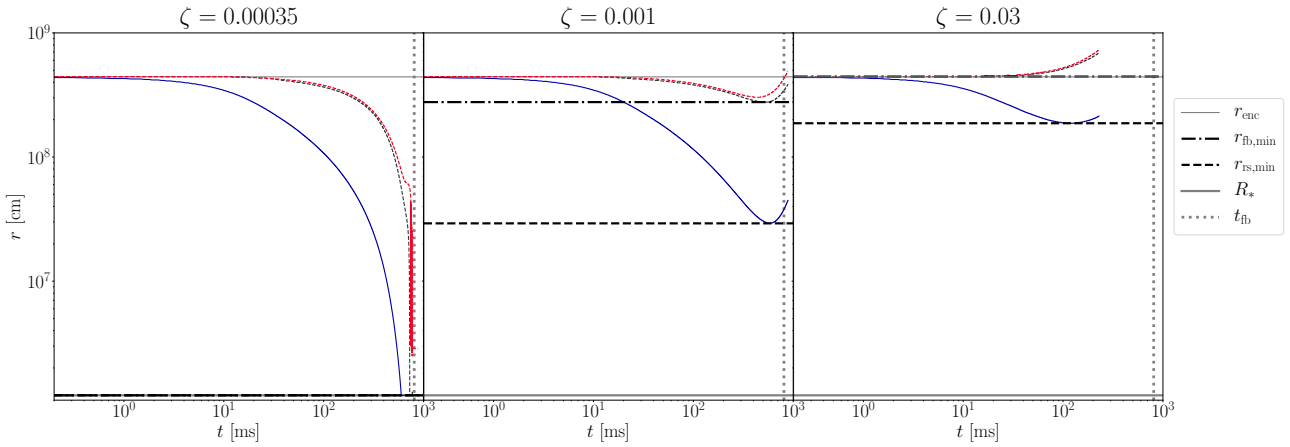

(a) $\zeta < \zeta_{\rm min}$ (b) $\zeta_{\rm min} < \zeta < \zeta_{\rm cri}$ (c) $\zeta > \zeta_{\rm cri}$

Figure 3.3: Time evolution of the shock structure of the case shown in Fig. 3.2. The left panel shows how fallback matter successfully invade down to the NS surface in intense fallback limit ($\zeta < \zeta_{\rm min}$), where the opposite end with $\zeta > \zeta_{\rm cri}$ presents how the outflow completely repell the fallback matter (see the right panel). The intermediate case with $\zeta_{\rm min} < \zeta < \zeta_{\rm cri}$ is shown in the the center panel, where the fallback matter initially invade into the outflow but becomes overwhelmed before reaching the NS surface. Here the shocked region is bounded by the forward shocks (red dashed lines) and reverse shocks (blue solid lines) as the shaded regions; The thin grey and thick grey solid lines stand for the encounter radius and NS surface, respectively.

both the minimum position of the fallback radius $r_{\rm fb,min}$ and the reverse shock front $r_{\rm rs,min}$ are non-trivial: since the former one is especially important for characterizing the shock dynamics and determining the fate of the central young NS, we carried out a series of simulations to investigate its dependence on the parameter space we are interested in. Fig. 3.4 summarizes the results for the fallback-outflow systems encounter at $r_{\rm enc} = 4.5 \times 10^7$ cm and 4.5×10^8 cm with different energy flux ratios ζ, in which the upper and lower out- to inflow luminosity bound for $r_{\rm fb,min}$ to be non-trivial are found to be $\zeta_{\rm cri}$ and $\zeta_{\rm min}$, respectively. It is them who separates the the accretion shock dynamics shown in Fig. 3.2 and 3.3 into three different types as mentioned above.

Firstly, $\zeta_{\rm cri}$ distinguishes the systems with monotonically expanding accretion shock (i.e., $\zeta > \zeta_{\rm cri}$) and the one that initially contrasts. As for the former cases, the ram pressure of the relativistic wind should overwhelm that of the fallback inflow while encountering in order to make the shock expanding. In other words, the critical value $\zeta_{\rm cri}$ can be analytically derived from the ram pressure balance at the encounter radius as

$$\frac{L}{4\pi {r_{\rm enc}}^2 c} \gtrsim \frac{\dot{M}_{\rm fb,ini} v_{\rm fb}(r_{\rm enc})}{4\pi {r_{\rm enc}}^2}, \tag{3.1}$$

or

$$\zeta \gtrsim \zeta_{\rm cri} = \left(\frac{2GM_*}{r_{\rm enc} c^2} \right)^{1/2}. \tag{3.2}$$

Note that Eq. (3.2), as shown with dotted lines in Fig. 3.4, is consistent with our numerical results.

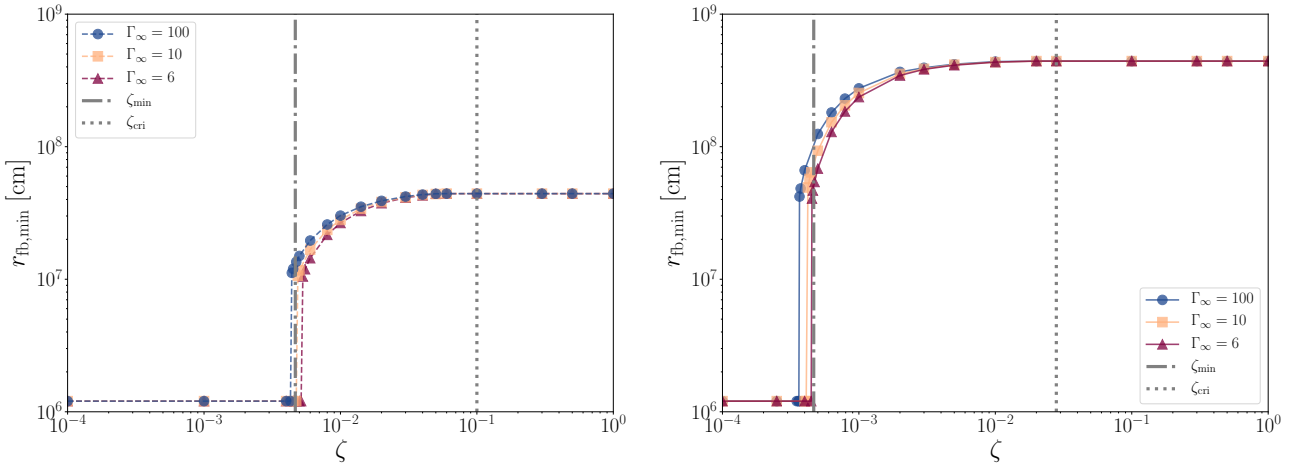

(a) $r_{\rm enc} = 4.5{\times}10^7$ cm (b) $r_{\rm enc} = 4.5{\times}10^8$ cm

Figure 3.4: Dependence of the minimum fallback radius $r_{\rm fb,min}$ on the energy flux ratio ζ. The fallback-outflow systems encounter at $r_{\rm enc} = 4.5 \times 10^7$ cm (dashed data curve) and 4.5×10^8 cm (solid data curve) with terminal Lorentz factor of outflow $\Gamma_\infty = 6$ (wine triangle-up points), 10 (peach square points) and 100 (cobalt circle points) are shown. Two critical values that separate the three different shock dynamics $\zeta_{\rm cri}$ (Eq. 3.2) and $\zeta_{\rm min}$ (Eq. 3.3) are marked by the vertical dotted and dashed lines, respectively.

For the cases with $\zeta < \zeta_{\rm cri}$, the minimum fallback radius is proved to be positively related to the energy ratio, and evolves exponentially regarding ζ around another critical value $\zeta_{\rm min}$, where the system with $\zeta < \zeta_{\rm min}$ satisfies that $r_{\rm fb,min} = r_{\rm rs,min} = R_*$. This critical value serves as the lower bound of the fallback-outflow system with the accretion shock to be initially contracting but expanding later, and its dependence on the encounter radius and the terminal Lorentz factor of the outflow are summarized in Fig. 3.5.

The numerical results indicate that $\zeta_{\rm min}$ should be inversely proportional to $r_{\rm enc}$ as

$$\zeta_{\rm min} \approx \frac{GM_*}{c^2 r_{\rm enc}}, \tag{3.3}$$

which can be analytically explained by our simplified thin-shell model in Appendix A. We assume that the shocked matter can be modeled as a thin shell at the contact surface $r_{\rm fb}$, in which its dynamics is governed by the simplified hydrodynamics equations with taken account in the central gravity. In that sense, the system with time-integrated outflow luminosity comparable to the the gravitational work being exerted to the shocked matter at about one fallback time scale corresponds to the critical situation that the fallback accretion is marginally repelled, i.e., $\zeta \approx \zeta_{\rm min}$; below which the outflow will not be energetic enough to play against the fallback matter at the time when gravity becomes increasingly significant. This result, which can be both derived by analytical model and numerical studies (see Eq. (3.3)), is also broadly in agreement with what given by self-similar study towards the expanding accretion shock to ensure the existence of self-similar solutions [2].

From the cases with three different outflow Lorentz factors $\Gamma_\infty = 6$, 10, and 100 shown in Figs.

[2]See Shigeyama & Kashiyama (2018) and their Eq. 31 and 32, where the dimensionless energy flux ratio is defined as $4\pi D_{\rm fs}\sqrt{\xi_{\rm s}}$ in their Eq. (27).

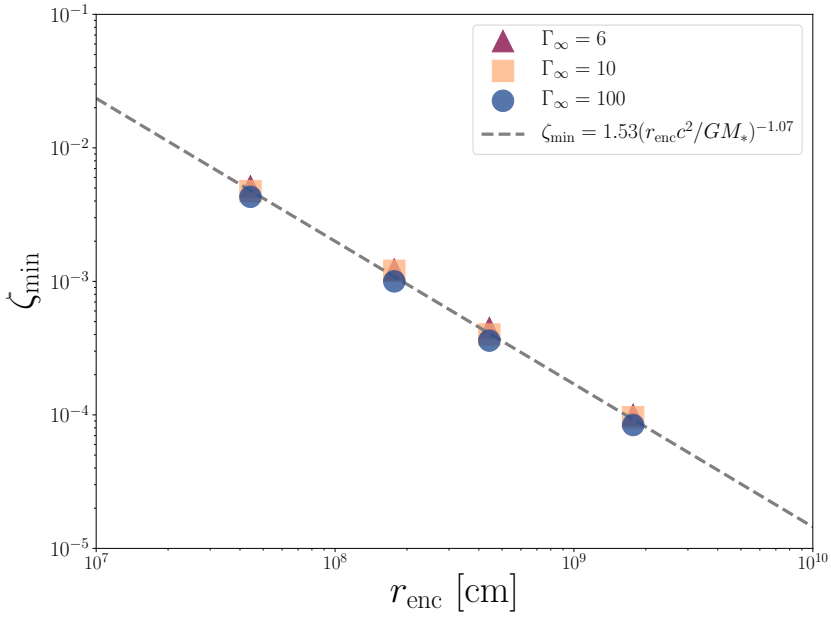

Figure 3.5: Dependence of the largest energy flux ratio for the fallback matter to successfully invade down to the NS surface $\zeta_{\rm min}$ on the parameter space of encounter radius and the terminal Lorentz factor of the outflow. Three different wind Lorentz factor are considered: $\Gamma_\infty = 6$ (wine triangle-up points), 10 (peach square points) and 100 (cobalt circle points); while the dashed line corresponds to Eq. (3.3).

3.4 and 3.5, we conclude that $r_{\rm fb,min}$ and so as $\zeta_{\rm min}$ hardly vary with Γ_∞ [3]. Since the minimum fallback radius $r_{\rm fb,min}$ is defined when the time-integrated outflow luminosity is marginally comparable to the gravitational work exerted to the shocked matter, and neither of them is affected by the outflow velocity in the relativistic regime, Eq. (3.3) can be safely applied to the systems with a higher terminal Lorentz factor of outflow regardless of the upper bound of our parameter space of exploring $\Gamma_\infty \leq 100$.

To the end, we shall note that the contact surface in the contracting phase is always subject to the Rayleigh-Taylor (RT) instability given the velocity, density and pressure profiles we set (Appendix B). The so-called RT fingers will be developed when the RT instability is being induced, which breaks the spherical symmetry in both fallback accretion and relativistic outflow region particularly in the cases around the critical condition $\zeta \approx \zeta_{\rm min}$. This will be discussed and further investigated in Sec. 4 and 5.

[3] We also confirm that the results hold for a mildly relativistic case with e.g., $\Gamma_\infty = 2$

Chapter 4

Implications for the diversity in young neutron stars

In Sec. 3, we obtain a necessary condition for supernova fallback confronting with a relativistic outflow at the initial fallback radius $r_{\rm enc}$ (Eq. 2.15) to reach the near NS surface region as $\zeta < \zeta_{\rm min}$ (see Eq. 3.3), which will be our starting point to discuss the bifurcation into RPPs with force-free magnetosphere and magnetars/CCOs with disturbed/buried magnetosphere. Since

$$\zeta_{\rm min} = \frac{L}{\dot{M}_{\rm fb,crit} c^2}, \tag{4.1}$$

where $\dot{M}_{\rm fb,crit}$ stands for the critical mass accretion rate for the fallback accretion to reach down to the near NS surface region under the outflow luminosity L given by certain field configuration , the total fallback mass in this critical situation can be described in terms of the fallback time $t_{\rm fb}$ and the outflow luminosity L as

$$M_{\rm fb,crit} \approx \frac{5}{2} \times (GM_*)^{-2/3} L {t_{\rm fb}}^{5/3}. \tag{4.2}$$

Considering the magnetosphere before fallback sets in to be a rotating dipole radiation (Gruzinov, 2005; Spitkovsky, 2006; Tchekhovskoy et al., 2013), the outflow luminosity can be estimated as

$$L_{\rm d} = \frac{{B_*}^2 {\Omega_{\rm i}}^4 R_*^6}{4c^3} (1 + \sin\chi^2) \sim 4.3 \times 10^{41}\,{\rm erg\,s^{-1}}\,(1+\sin\chi^2)\,{B_{*,13}}^2 {P_{\rm i,-2}}^{-4}, \tag{4.3}$$

where B_*, R_* and $\Omega_{\rm i}$ are the surface field strength, the radius and the initial angular frequency of NSs, and χ stands for the inclination angle between the dipole and rotation axes. With rotational energy of NSs $E_{\rm rot}$ shown in Eq.(1.2), the spin-down time scale can be thus estimated as

$$t_{\rm sd} \sim \frac{E_{\rm rot}}{L_{\rm d}} = 23.5\,{\rm yr}\,(1+\sin\chi^2)^{-1} {B_{*,13}}^{-2} {P_{\rm i,-2}}^2, \tag{4.4}$$

which is much more longer than the free-fall time scale we are interested in (see Sec. 2.1.3). Under this circumstance, the critical fallback mass to reach the near NS surface region under the undisturbed dipole field configuration can be obtained by substituting Eq. (4.3) to Eq. (4.2) as

$$M_{\rm fb,crit} \approx 7.7 \times 10^{-8}\,M_\odot\,(1+\sin\chi^2)\,{B_{*,13}}^2 {P_{\rm i,-2}}^{-4} {t_{\rm fb,1}}^{5/3} \quad \text{(dipole)}. \tag{4.5}$$

The fallback matter with the total mass $M_{\rm fb} \lesssim M_{\rm fb,crit}$ will be repelled by the dipole spin-down power (see the central and right panel of Fig. 3.2), in which the magnetosphere will be force-free; otherwise it keeps invading in as shown in the left panel of Fig. 3.2. Note that this kind of invasion will be mostly in an anisotropic manner (see Sec. 5.2.3), where there always exists the most advanced flow that channels to the near NS surface region; the contact surface that is subjected to the R-T instability (see Appendix B), in which the R-T finger will then compress the magnetosphere at that direction down to the size in which magnetic pressure becomes comparable with the ram pressure of the accreting matter, i.e. the Alfvén radius as

$$r_{\rm A} = \left(\frac{{B_*}^2 {R_*}^6}{\dot{M}_{\rm fb}\sqrt{2GM_*}}\right)^{2/7} \sim 1.1\times10^6\,{\rm cm}\,{B_{*,13}}^{4/7}{M_{\rm fb,-4}}^{-2/7}{t_{\rm fb,1}}^{2/7}, \tag{4.6}$$

which is generally smaller than the light cylinder (Eq. 1.13) and the co-rotation radius

$$r_{\rm co} = \left(\frac{GM_*}{{\Omega_{\rm i}}^2}\right)^{1/3} \sim 7.8\times10^6\,{\rm cm}\,{P_{\rm i,-2}}^{2/3} \tag{4.7}$$

in the cases of our interest. As mentioned in Sec. 1.3, this kind of anisotropic accretion will enhance the spin-down torque of the NS mainly through expanding the polar cap region of open magnetic field lines (e.g., Parfrey et al., 2016; Metzger et al., 2018); where the enhanced outflow luminosity can be described as

$$L_{\rm m} \approx \begin{cases} ({B_*}^2{\Omega_{\rm i}}^4 R_*^6/c^3)\times(r_{\rm lc}/r_{\rm A})^2 \sim 3.1\times10^{45}\,{\rm erg\,s^{-1}}\,{B_{*,13}}^{6/7}{P_{\rm i,-2}}^{-2}{M_{\rm fb,-4}}^{4/7}{t_{\rm fb,1}}^{-4/7} & r_{\rm A} > R_* \\ ({B_*}^2{\Omega_{\rm i}}^4 R_*^6/c^3)\times(r_{\rm lc}/R_*)^2 \sim 2.7\times10^{45}\,{\rm erg\,s^{-1}}\,{B_{*,13}}^2{P_{\rm i,-2}}^{-2} & r_{\rm A} \le R_* \end{cases}, \tag{4.8}$$

with the latter case corresponding to the split monopole configuration that yields the possible maximum power for a given set of B_* and $P_{\rm i}$. The bulk of the fallback matter aside of those accreted through the advanced channeled flows will confront with this enhanced outflow, which leads to a new critical total fallback mass for the fallback accretion to reach down to the near NS surface region and continuously disturb the magnetosphere as

$$M_{\rm fb,crit} \approx \begin{cases} 5.2\times10^{-3}\,M_\odot\,{B_{*,13}}^2{P_{\rm i,-2}}^{-14/3}{t_{\rm fb,1}}^{23/9} & r_{\rm A} > R_* \\ 4.8\times10^{-4}\,M_\odot\,{B_{*,13}}^2{P_{\rm i,-2}}^{-2}{t_{\rm fb,1}}^{5/3} & r_{\rm A} \le R_* \end{cases}. \tag{4.9}$$

Similar to what is given by Eq. 4.5, the fallback matter with total mass smaller than Eq. (4.9) will be repelled by the enhanced spin-down power and eventually leave a force-free magnetosphere; otherwise the newly formed magnetosphere is expected to be strongly disturbed and polluted by the fallback accretion. In particular, the fallback matter can enshroud and bury the surface magnetic fields if the total mass is greater than Eq. (4.9) with

$$r_A \le R_*, \tag{4.10}$$

or

$$M_{\rm fb} > 8.2\times10^{-5}\,M_\odot\,{B_{*,13}}^2 t_{\rm fb,1}. \tag{4.11}$$

The above discussions are summarized in Fig. 4.1. The dotted and solid line indicate the two critical condition given by $\zeta_{\rm min}$ under different field configuration corresponded to Eq. (4.5) and Eq. (4.9), which together indicate the bifurcation into RPPs and magnetars/CCOs; and the dashed line shows the boundary set by Eq. (4.11), which further clarifies the boundary

between magnetars and CCOs. In detail, for the cases that reside

- below the solid line: either the dipole radiation or enhanced spin-down power sweeps out the fallback accretion, though it may wait until the channel flow to the pole region ceases to restore a force-free magnetosphere for the latter case. NSs with the surface magnetic field and rotation period within this parameter regime naturally evolve into RPPs.
- above the dashed line: the fallback accretion is intense enough for burying the surface magnetic fields under the outer crust, which results into significantly weak apparent magnetic field. NSs with the surface magnetic field and rotation period within this parameter regime can potentially be observed as CCOs.
- above the solid line but below the dashed line: the fallback accretion can invade down to the NS surface without completely burying the surface magnetic fields, which leads to a strongly disturbed magnetosphere in a chaotic manner within a fallback timescale. Although addressing the resultant magnetosphere structure in detail is beyond the scope of one dimensional hydrodynamics study, we propose this kind of quasi-spherical compression of the rotating magnetosphere to be potentially responsible of amplifying the magnetic field strength through synthesizing multipolar magnetic fields, in addition to the dynamo-like activities (see Sec. 1.3) in the core-collapse and the proto-NS phase. Since this scenario does not require the central NS to be born with ultra-strong magnetic fields ($\sim 10^{14}$-10^{16} G), it would serves as a more natural option to form a magnetar.

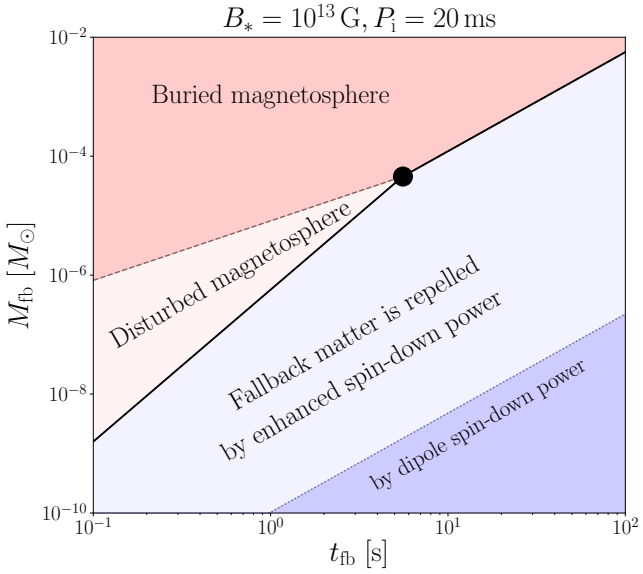

Figure 4.1: Possible consequences of the collision between rotation-powered wind from a newborn neutron star with a surface magnetic field $B_* = 10^{13}$ G and an initial spin period $P_\mathrm{i} = 20$ ms and supernova fallback with total fallback mass M_fb and fallabck timescale t_fb.

In the proposed scenario, the branching into three different NS populations occurs at the intersection of the solid and dashed lines in Fig. 4.1 as marked by a black point with critical magnetic field

$$B_{*,\mathrm{tri}} \approx 1.1 \times 10^{13}\,\mathrm{G}\, {M_{\mathrm{fb},-4}}^{1/2} {t_{\mathrm{fb},1}}^{-1/2} \tag{4.12}$$

and initial rotation period

$$P_{\mathrm{i,tri}} \approx 24\,\mathrm{ms}\, t_{\mathrm{fb},1}^{1/3}; \tag{4.13}$$

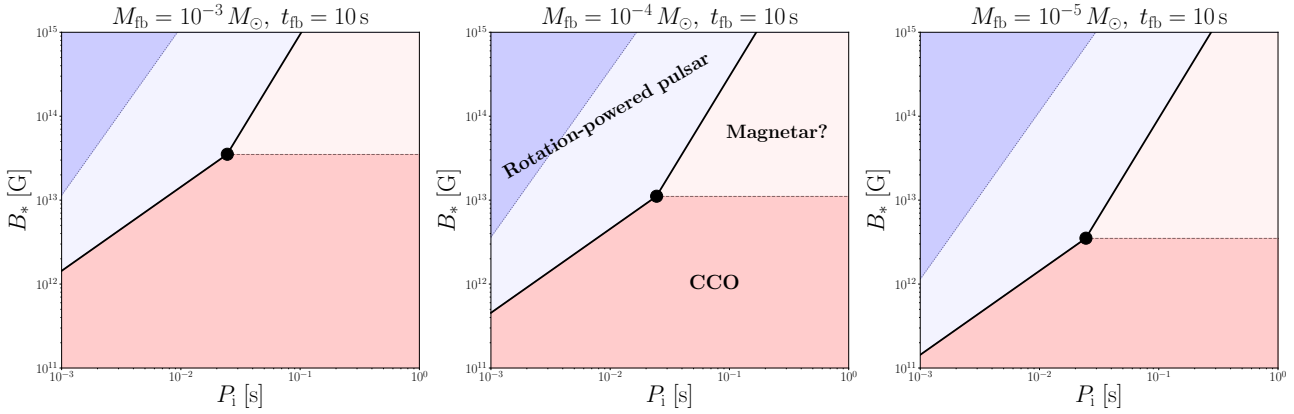

Figure 4.2: Possible trifurcation in the types of neutron star caused by the interaction between the rotation-powered wind and the supernova fallback in the newborn phase. The left, center, right panels show the cases with fixed fallback time $t_{\rm fb} = 10\,{\rm s}$ and fallback mass of $M_{\rm fb} = 10^{-3}\,M_\odot$, $10^{-4}\,M_\odot$, $10^{-5}\,M_\odot$, respectively.

where $P_{\rm i,tri}$ does not depend on the fallback mass. Our proposed scenario gives several implications that can be tested by observational facts as follows:

1) For a typical range of the fallback accretion with $M_{\rm fb} \sim 10^{-2}$-$10^{-4}\,M_\odot$ and $t_{\rm fb} \sim$ 1-100 s, Eq. (4.12) and (4.13) imply a trifurcation occurring at $B_* \sim 10^{13}\,{\rm G}$ and $P_{\rm i} =$ a few 10 ms (see Fig. 4.2). Such a magnetic field strength and rotation period at birth are not only broadly consistent with those inferred as Galactic rotation-powered pulsars (see Sec. 1.2.1), i.e., a typical pulsar formation occurs at around the triple point; but also can naturally explain the observed fact that the formation rate of rotation-powered pulsars may roughly be comparable to those of CCOs and magnetars (~ 1 century^{-1}, e.g., Keane & Kramer, 2008, see Sec. 1.2 for reference as well).

2) The boundary between CCOs and magnetars is relatively blur; the newborn NS with magnetic field and rotation period around the grey dotted line in Fig. 4.2 can potentially hold the properties from both of them (e.g., 1E 161348-5055 at the centre of SNR RCW103 that is categorized into CCO but has the magnetar-like activities, see Tuohy & Garmire, 1980). In this sense, our scenario prefers the foster formation scheme that magnetars are born with mildly strong magnetic field ($\sim 10^{12}$-10^{13} G) with amplifying by the prompt fallback accretion rather than the ultra-strong magnetic field being observed so far ($\sim 10^{14}$-10^{16} G).

3) As implied by Fig. 4.2, the system with larger total fallback mass $M_{\rm fb}$ is more likely to produce a CCO or magnetar. Since $M_{\rm fb}$ is considered to be positively correlated to the progenitor mass, this suggests the progenitor of magnetars/CCOs to be possibly more massive than that of pulsars, which is broadly consistent with the current observation: the progenitor of a magnetar is considered to be a massive star with zero-age main sequence mass $M_{\rm ZAMS} \gtrsim$ 30-40 $M_\odot$ in the conventional magnetar model (e.g., Enoto et al., 2019), and the observational constraints suggest the main sequence progenitor mass of the CCO associated with Cas A to be 15-20 $M_\odot$ (e.g., Young et al., 2006); while the progenitor mass of Crab-like pulsar is considered to be $M_{\rm ZAMS} \sim$ 8-10 $M_\odot$ (e.g., Nomoto et al., 1982).

Chapter 5

Conclusion and Discussion

In this chapter, we will briefly summarize our work done in Sec. 3 and Sec. 4, and discuss the problem left for the future study in Sec. 5.1; in which as a preparation, the first-stage results given by 2-D RHD study are presented in 5.2: Sec. 5.2.1 shows the imprints of 1-D RHD study in spherical 2-D RHD study; while Sec. 5.2.2 and Sec. 5.2.3 mainly investigates the effect of non-spherical effects on the evolution of accretion shock structure. Finally, the critical condition for the fallback accretion to invade down to the magnetosphere of young NS under 2-D RHD study will be shown in Sec. 5.2.4.

5.1 Summary and discussion

In this work, in order to investigate the effect of fallback accretion together with the outflow from the young NSs magnetosphere on their diversity, we perform a 1-D RHD simulations of fallback accretion confronting with the relativistic outflow.

We firstly show how the colliding systems with different out- to inflow luminosity ratio ζ evolves with time in Fig. 3.2: after simulation starts, multiple discontinuities including reverse shock, forward shock and contact surface form into the accretion shock structure. We note that the fallback radius can be regarded as the position of contact surface here, which is supposed to be mostly subjected to Rayleigh-Taylor instability (see App. B, though can not be captured by one dimensional study), and the dynamical evolution of fallback radius can be categorized into three categories regarding the energy flux ratio of the system ζ: the fallback matter monotonically expands for the systems with $\zeta > \zeta_{\rm cri}$ (e.g., see the right column of Fig. 3.3), while monotonically contracts down to the stellar surface R_* if $\zeta < \zeta_{\rm min}$ (e.g., see the left column of Fig. 3.3). Otherwise it initially contracts to the minimum fallback radius $r_{\rm fb,min}$ and bounces back in the intermediate regime $\zeta_{\rm min} \lesssim \zeta \lesssim \zeta_{\rm cri}$ (e.g., see the central column of Fig. 3.3), where the $\zeta_{\rm cri}$ that separates the monotonically-expanding cases from the intermediate cases can be analytically obtained through the initial momentum balance at the encounter radius in Eq.(3.1).

Since the minimum fallback radius $r_{\rm fb,min}$ would only be non-trivial for the systems with $\zeta_{\rm min} \lesssim \zeta \lesssim \zeta_{\rm cri}$ ($r_{\rm fb,min} = r_{\rm enc}$ and R_* while $\zeta > \zeta_{\rm cri}$ and $\zeta < \zeta_{\rm min}$ according to the definition, respectively), we showed its dependence on out- to inflow luminosity ratio ζ and Lorentz

factor of outflow at infinity Γ_∞ for two different encounter radius $r_{\rm enc}$ in Fig. 3.4. Simulation results imply the minimum fallback radius $r_{\rm fb,min}$ to be positively correlated to ζ while just moderately depends on Γ_∞; and the $\zeta_{\rm min}$ where $r_{\rm fb,min}$ begins to decrease exponentially with ζ marks the situation for the fallback matter to successfully invade down to the stellar surface. Numerically we find that $\zeta_{\rm min}$ can be inverse-proportionally fitted regarding the encounter radius $r_{\rm enc}$ (see Fig. 3.5) as $\zeta_{\rm min} \propto r_{\rm enc}^{-1}$, which can be analytically explained as the equilibrium between the time-integrated outflow luminosity the gravitational work exerted to the flows (see App. A). This energy points of view also evidence the fact that the minimum fallback radius $r_{\rm fb,min}$ barely changes with the terminal outflow Lorentz factor Γ_∞, which mainly serves as a baryon loading parameter.

Combining with the outflow luminosity under different field configuration and the condition for the fallback matter to bury the NS surface magnetic field, the criterion for the fallback matter to reach down to the near stellar surface region (see Eq.(4.2)) gives the physical picture of NSs to trifurcate into RPPs, magnetars and CCOs, as schematically shown in Fig. 5.1. In this proposed scenario, the trifurcation point of rotation-powered pulsars, magnetars and

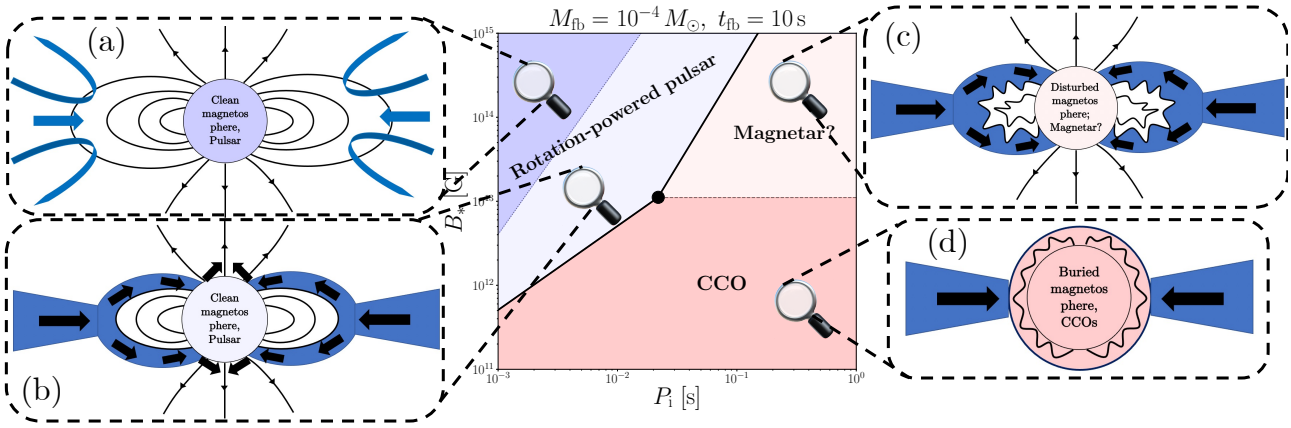

Figure 5.1: Schematic picture of possible trifurcation of neutron star caused by the interaction between the rotation-powered wind and the supernova fallback in the newborn phase, followed the fallback accretion parameter shown in the central panel of Fig. 4.2 ($t_{\rm fb} = 10\,{\rm s}$, $M_{\rm fb} = 10^{-4}\,M_\odot$). Where block (a) and (b) shows the situation with the fallback accretion being repelled either by the non-disturbed dipole radiation or a monopole-like radiation of the field that is maximumly-opened by the anisotropic invasion of fallback accretion; which all lead to the formation of RPPs with force-free magnetosphere eventually. On the other hand, the newly formed magnetosphere would be strongly disturbed or even buried under the prompt fallback crust if the enhanced torque due to the anisotropic accretion still fail to repel the fallback matter, which potentially leads to the formation of magnetars and CCOs as shown in block (c) and (d), respectively.

CCOs (see the black solid dot in Fig. 4.2) roughly lies in the regime where magnetic field strength $B_* \sim 10^{13}$ G and rotation period $P_i \sim O(10)$ ms at birth assuming typical range of fallback accretion, which is broadly consistent with the Galactic rotation-powered pulsars (e.g., Crab-like Pulsar), and can naturally leads to a potentially comparable formation rate among rotation-powered pulsar, CCOs and magnetars. In addition, a more massive progenitor for magnetar may also be implied.

Finally, we shall notice that since we mainly carried out the simulation under spherical symmetry, multi-dimensional studies are desirable for taking varies important processes (e.g., the

RT instability developed at the contact surface, the anisotropic way of proceeding for fallback accretion and outflow from the NS magnetosphere) into account. Furthermore, magnetohydrodynamics simulations are also of great importance especially for the cases where the fallback matter successfully proceed down to the near stellar surface region and compress the magnetosphere of NS: how the field lines are expanded by this kind of accretion, whether the multi-polar magnetic field will be synthesized and thus amplify the apparent magnetic field strength when it is strongly disturbed still remain as open questions. Numerical simulations as well as the analytical work within this parameter regime shall be especially helpful for us to test our formation scheme of both magnetars and CCOs.

5.2 Future Work

As noted in Sec. 5.1, our numerical results are obtained by spherically symmetric RHD simulations. However the fallback accretion and the relativistic outflow from the nascent NS magnetosphere are in general anisotropic, and the contact surface between the in- and outflows will be subjected to the RT instability, which the consequences cannot be captured by our one-dimensional study. Multi-dimensional simulations are desirable for quantifying the effects of these factors on the NS diversity, and some results at the first stage are presented as follows.

5.2.1 Spherical 2-D relativistic hydrodynamics correspondence

We first checked the consistency between the results given by 1-D and 2-D spherical simulations under $r_{\rm enc} = 4.5 \times 10^7$ cm.

From Eq.(2.28)-(2.29), we can firstly write down the governing equations for 2-D RHD study as:

$$\partial_t D + \frac{1}{r^2}\partial_r\left(r^2 D v^r\right) + \frac{1}{r\sin\theta}\partial_\theta\left(D v^\theta \sin\theta\right) = 0 \tag{5.1}$$

$$\partial_t S_r + \frac{1}{r^2}\partial_r\left\{r^2\left(v^r S_r\right)\right\} + \partial_r p + \frac{1}{r\sin\theta}\partial_\theta\left\{\left(v^\theta S_r\right)\sin\theta\right\} - \frac{v^\theta S_\theta}{2r} = -\frac{GM_*}{r^2}D \tag{5.2}$$

$$\partial_t S_\theta + \frac{1}{r^2}\partial_r\left\{r^2\left(v^r S_\theta\right)\right\} + \frac{1}{r\sin\theta}\partial_\theta\left\{\left(v^\theta S_\theta\right)\sin\theta\right\} + \frac{1}{r}\partial_\theta p + \frac{v^r S_\theta}{2r} = 0 \tag{5.3}$$

$$\partial_t E + \frac{1}{r^2}\partial_r\left\{r^2 S_r\right\} + \frac{1}{r\sin\theta}\partial_\theta\left\{S_\theta\sin\theta\right\} = -\frac{GM_*}{r^2}S_r \tag{5.4}$$

Where

$$D = \Gamma\rho, \tag{5.5}$$

$$S_r = \Gamma^2\rho h\beta^r = \Gamma^2\rho h v^r, \tag{5.6}$$

$$S_\theta = \Gamma^2\rho h\beta^\theta = \Gamma^2\rho h v^\theta, \tag{5.7}$$

$$E = \Gamma^2\rho h - p, \tag{5.8}$$

with ρ, β^r, β^θ, p being proper mass density, velocity at radius direction, velocity at θ direction, and gas pressure, respectively; while Γ and h stand for the Lorentz factor and special enthalpy shown in Eq.(2.30) and (2.33). Here we take light speed $c = 1$.

The numerical set-ups for 2-D spherical simulation are basically the same as 1-D except for the mesh number on the θ direction (see Fig. 5.2). In 2-D testing cases, we set its fiducial value as 64 here. In order to avoid the carbuncle instability (e.g., Pandolfi & D'Ambrosio, 2001) that mainly occurs due to the lack of consideration on the shear viscosity (in this case, terms related to $\partial_\theta v_r$) of Riemann solvers, we employ the HLLE solver instead of HLLC solver in 1-D simulation.

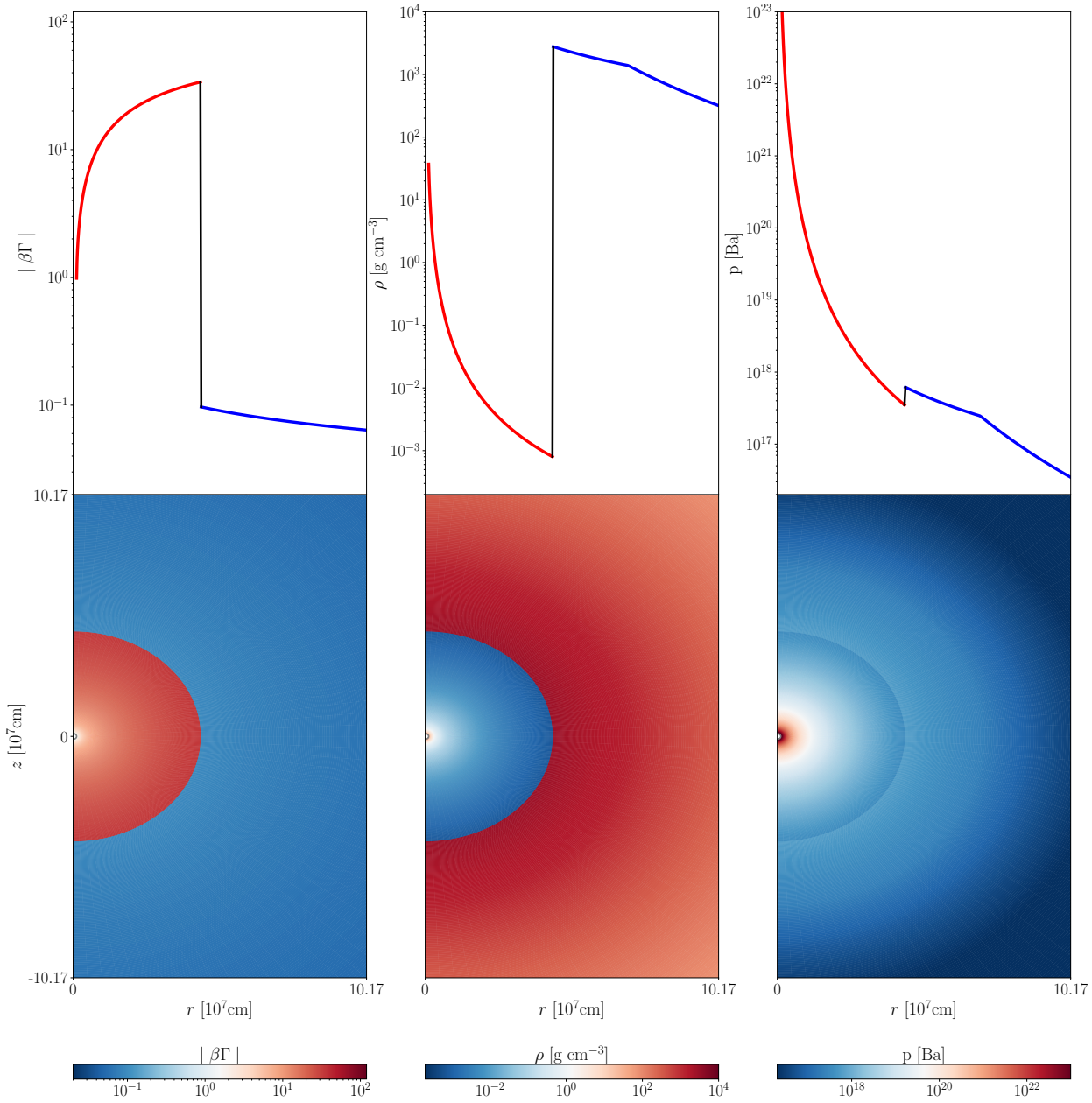

Figure 5.2: Comparison between numerical set-ups for 2-D (see the bottom row) and 1-D (see the top row) spherical simulations with out- to inflow luminosity ratio $\zeta = 0.01$ and terminal Lorentz factor of outflow $\Gamma_\infty = 100$ under $r_{\rm enc} = 4.5 \times 10^7$ cm: The left, central and right panel show the velocity, density and pressure profile, respectively.

As for the boundary condition, We set it to be so-called polar-wedge in the θ direction (as shown in Eq.(5.9)-(5.16)), where j loops from 1 to the number of ghost cells $N_{\rm ngh}$, jl and ju stand for the inner and outer most cell else than the ghost cells at inner and outer boundary of calculation domain, respectively.

$$v_{\rm r}^{i,jl-j,k} = v_{\rm r}^{i,jl+j-1,k}, \tag{5.9}$$

$$v_{\theta}^{i,jl-j,k} = -v_{\theta}^{i,jl+j-1,k}, \tag{5.10}$$

$$\rho^{i,jl-j,k} = \rho^{i,jl+j-1,k}, \tag{5.11}$$

$$p^{i,jl-j,k} = p^{i,jl+j-1,k}, \tag{5.12}$$

$$v_{\rm r}^{i,ju+j,k} = v_{\rm r}^{i,ju-j+1,k}, \tag{5.13}$$

$$v_{\theta}^{i,ju+j,k} = -v_{\theta}^{i,ju-j+1,k}, \tag{5.14}$$

$$\rho^{i,ju+j,k} = \rho^{i,ju-j+1,k}, \tag{5.15}$$

$$p^{i,ju+j,k} = p^{i,ju-j+1,k}. \tag{5.16}$$

while the boundary condition for radius direction shown in Eq.(2.16)-(2.27) shall include the velocity at θ direction v_θ as follows:

$$v_\theta(R_*, \theta) = 0, \tag{5.17}$$

$$v_{\theta}^{il-i,j,k} = 0, \tag{5.18}$$

$$v_\theta(r_{\rm out}, \theta) = 0, \tag{5.19}$$

$$v_{\theta}^{iu+i,j,k} = 0. \tag{5.20}$$

Given the mesh spacing, initial condition and boundary conditions shown as above, we found that the dynamical evolution of the accretion shock, together with the two critical values $\zeta_{\rm cri}$ and $\zeta_{\rm min}$, make no difference if one only set non-trivial mesh number on the θ direction without introducing any perturbation on the interface (or θ dependence of any physical parameters), as shown in Fig. 5.3.

5.2.2 2-D relativistic hydrodynamics study with non-spherical relativistic wind

In this section, we mainly investigate how the non-spherical relativistic outflow effects the dynamical evolution of the accretion shock. According to Tchekhovskoy et al. (2013), the

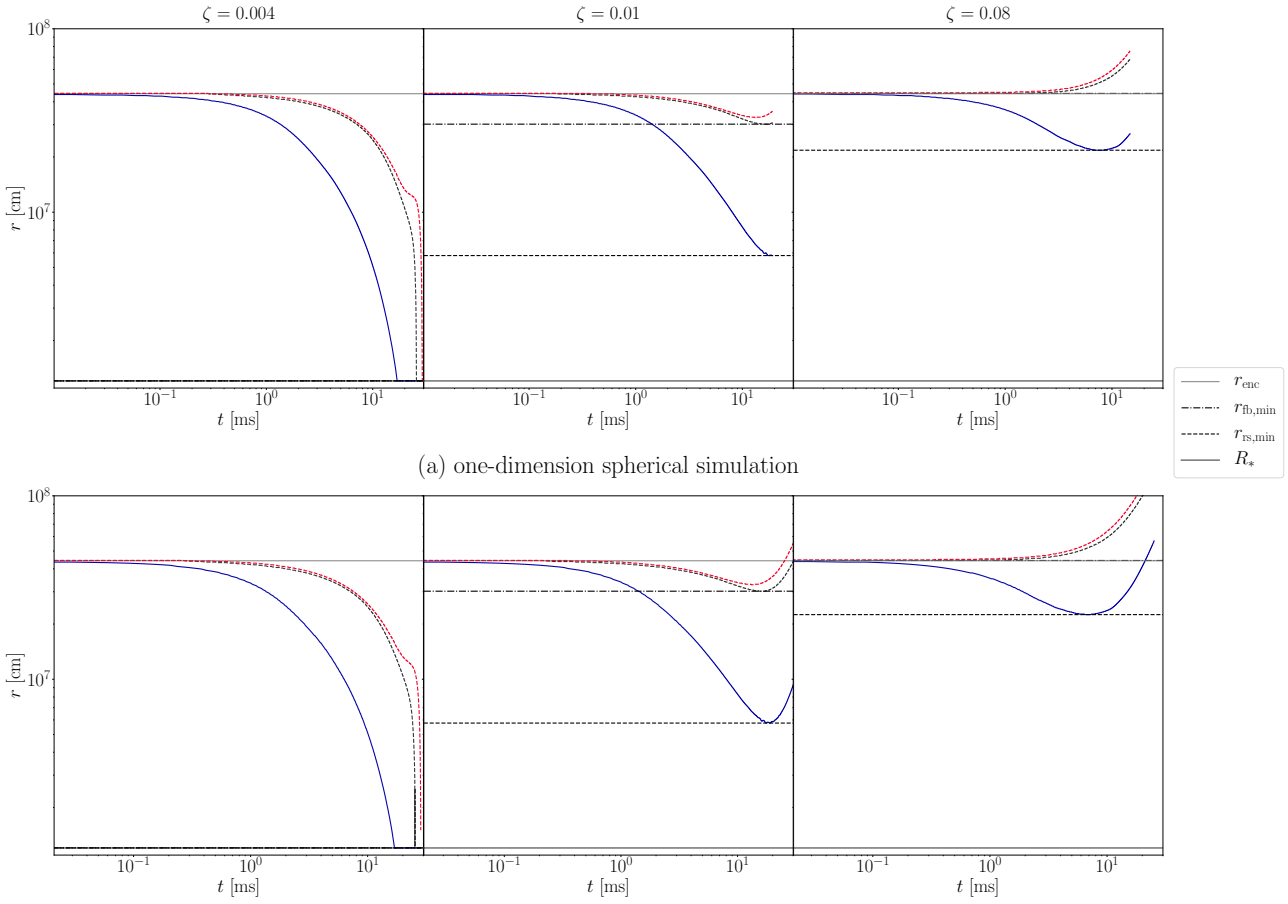

(a) one-dimension spherical simulation

(b) two-dimension spherical simulation

Figure 5.3: Comparison of dynamical evolution of accretion shock between 2-D (see the bottom row) and 1-D (see the top row) spherical simulations with out- to inflow luminosity ratio $\zeta = 0.004, 0.01, 0.08$ and terminal Lorentz factor of outflow $\Gamma_\infty = 100$ under $r_{\rm enc} = 4.5 \times 10^7$ cm: the shaded regions indicate the shocked region bounded by the forward shocks (red dashed lines) and reverse shocks (blue solid lines). The encounter radius and NS surface are marked by thin grey and thick grey solid line, respectively.

outflow luminosity $L_{\rm nph}$ shall be dependent on θ as

$$\frac{d^2L_{\rm tot}}{\sin\theta d\theta d\varphi} = L'\sin^4\theta \tag{5.21}$$

where $L^{'}$ here stands for the wind luminosity at the equatorial plane. We manually add a parameter δ in order to prevent any physical profiles from being 0 [1]:

$$\frac{d^2L_{\rm tot}}{\sin\theta d\theta d\varphi} = L'(\delta+\sin^4\theta), \tag{5.22}$$

where the fiducial value of δ is taken to be 0.1 in testing cases shown in this chapter. The total luminosity can be accordingly drafted as:

$$L_{\rm tot} = 2\pi L'\int_0^\pi \left(0.1+\sin^4\theta\right)\sin\theta d\theta. \tag{5.23}$$

Recalling that the total outflow luminosity $L_{\rm tot,\,sph}$ in the spherically symmetric cases (see Eq.(2.1)) can be written as:

$$L_{\rm tot,\,sph} = L \tag{5.24}$$

In order to maintain the out- to inflow luminosity ratio ζ, the total injected luminosity in both spherical and non-spherical simulations shall be set as equal:

$$L_{\rm tot} = L_{\rm tot,\,sph}, \tag{5.25}$$

or

$$\frac{L'}{L} = \frac{1}{2\pi\int_0^\pi\left(0.1+\sin^4\theta\right)\sin\theta d\theta} = 0.13. \tag{5.26}$$

The equations to be solved for determining the initial wind profile can be written as follows:

$$4\pi r^2\beta_{\rm w}{\Gamma_{\rm w}}^2\rho_{\rm w}h_{\rm w}c^3 = 1.58L(0.1+\sin^4\theta), \tag{5.27}$$

$$4\pi\Gamma_{\rm w}\beta_{\rm w}\rho_{\rm w}r^2c^3 = \frac{1.58L(0.1+\sin^4\theta)}{\Gamma_\infty}, \tag{5.28}$$

For each θ given by the mesh spacing, there exists an equivalent outflow luminosity $L_{\rm nph}$ at the RHS of Eq.(5.27) and (5.28):

$$L_{\rm nph} = \frac{4\pi}{2\pi\int_0^\pi\left(0.1+\sin^4\theta\right)\sin\theta d\theta}L(0.1+\sin^4\theta), \tag{5.29}$$

which can be used to determine the radii dependence of physical profiles at each θ direction.

Under this initial setting, the boundary conditions (see Eq.(5.9)-(5.16) for both the outer and inner boundary on θ direction, and Eq.(2.16)-(2.21) and (5.19)-(5.20) for the outer boundary condition on radius direction) should remain unchanged except for the inner boundary condition in radius direction:

$$v_{\rm r}(R_*,\theta) = 0.7c, \tag{5.30}$$

[1] It is generally to employ a floor value instead of setting physical profiles to be 0 since this is risky for numerical simulations.

$$v_\theta(R_*, \theta) = 0, \tag{5.31}$$

$$\rho(R_*, \theta) = \rho_{\rm w}(R_*, \theta) = \frac{L_{\rm nph}}{4\pi\Gamma_\infty\Gamma_{\rm w}(R_*, \theta)\beta_{\rm w}(R_*, \theta){R_*}^2 c^3}, \tag{5.32}$$

$$p(R_*, \theta) = p_{\rm w}(R_*, \theta) = \left[\left(\frac{\Gamma_\infty}{\Gamma_{\rm w}(R_*, \theta)} - 1\right)\frac{\gamma - 1}{\gamma}\right]\rho_{\rm w}(R_*, \theta)c^2, \tag{5.33}$$

with corresponding physical profiles fixed in the ghost cells:

$${v_{\rm r}}^{il-i,j,k} = 0.7c, \tag{5.34}$$

$$v_\theta^{il-i,j,k} = 0, \tag{5.35}$$

$$\rho^{il-i,j,k} = \rho_{\rm w}(R_*, \theta), \tag{5.36}$$

$$p^{il-i,j,k} = p_{\rm w}(R_*, \theta). \tag{5.37}$$

Where i loops from 1 to the number of ghost cells $N_{\rm ngh}$, and il stands for the inner most cell else than the ghost cells at the inner boundary.

As one may imagine, the shock produced under this physical setting will be anisotropic and can be especially strong among certain direction. In order to avoid the numerical crush while treating such a strong shock in 2-D study, we employ the HLLD Riemann solver with vanishing magnetic field in the whole computational regime (Mignone et al., 2009) and use the second-order piecewise linear reconstruction method (PLM) with minmod limiter (Roe, 1986) hereafter. The time integration is still carried out by the second order Runge-Kutta method with a Courant-Friedrich-Lewy number of 0.1. The computational domain is resolved with a non-uniform mesh [2] in radius direction and the mesh number of 256 that is uniformly spaced in θ direction in testing cases. Given the mesh spacing, we numerically set the initial profile with the cubic B spline (Burkardt, 2020) in the outflow region.

parameter	notation	range	unit
out- to inflow luminosity ratio	ζ	[0.004, 0.05, 1]	
outflow Lorentz factor at infinity	Γ_∞	100	
encounter radius	$r_{\rm enc}$	4.5×10^7	cm

Table 5.1: Run parameters in 2-D testing cases with non-spherical pulsar wind

We investigate the range of the parameters shown in Table 5.1. By detail, we choose the encounter radii as $r_{\rm enc} = 4.5 \times 10^7$ cm and terminal Lorentz factor as $\Gamma_\infty = 100$. For a given combination of $(r_{\rm enc}, \Gamma_\infty)$, we try three different ζ values that belong to different categories as shown in one-dimensional and spherical two-dimensional study (see Fig. 3.3 and 5.3). We fix the fallback accretion rate at $\dot{M}_{\rm fb,i} = 10^{-4}\, M_\odot\, {\rm s}^{-1}$ and vary the wind luminosity $L_{\rm nph}$ to change out- to inflow luminosity ratio ζ.

The results are shown in Fig. 5.4, Fig. 5.5 and Fig. 5.6. As one may notice, regardless of

[2] the fiducial value of the mesh number and grid size ratio $\Delta r(i+1)/\Delta r(i)$ is 512 and 1.007, respectively.

the fine structures forming in the shocked region, the final fate for the fallback accretion to be repelled or not has not changed. This is mainly due to the fact that the out- to inflow luminosity ratio ζ remains unchanged from the case with spherically symmetric outflow to the one with anisotropic outflow.

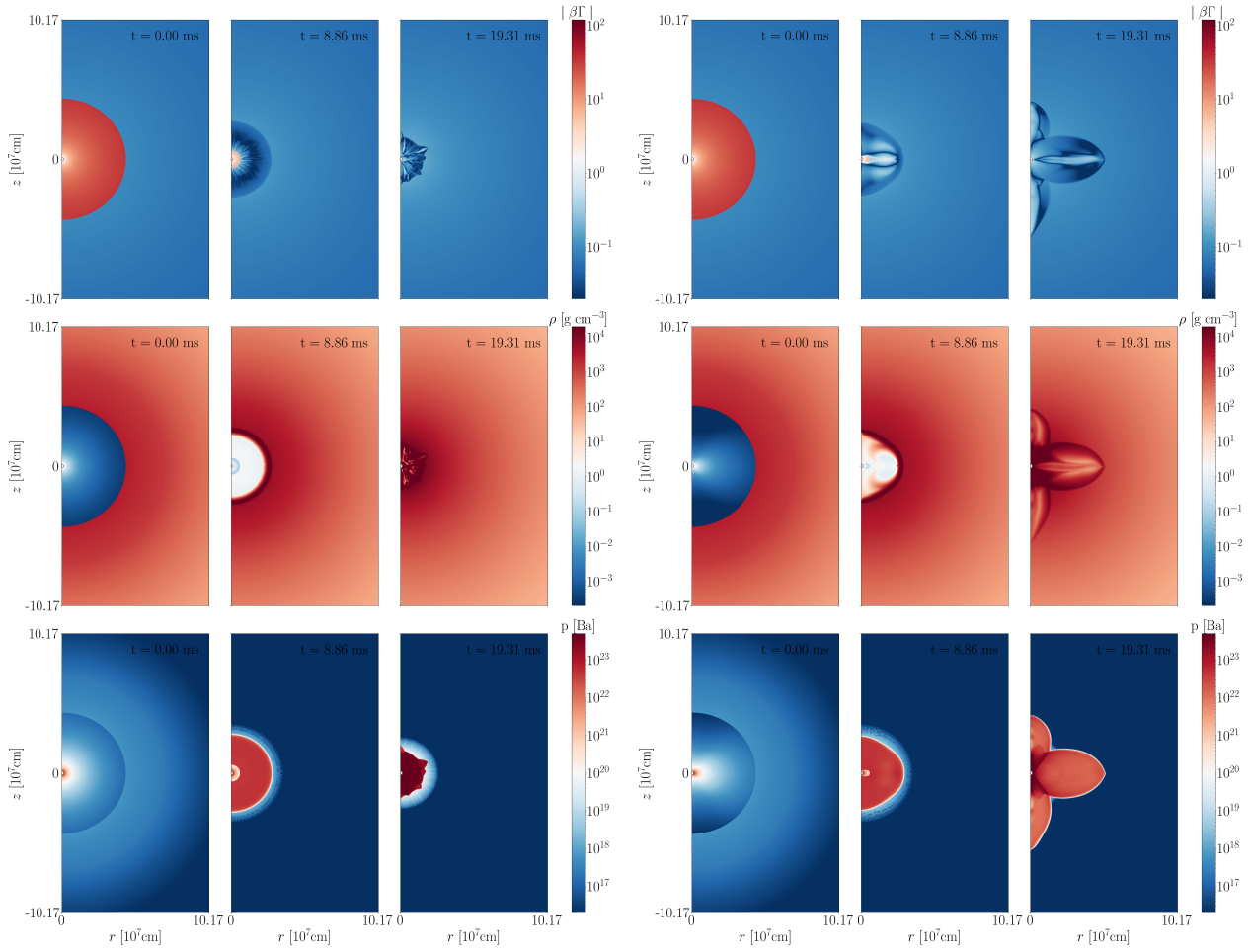

(a) $L = \text{const}$ (b) $L \propto (0.1 + \sin^4\theta)$

Figure 5.4: Comparison between dynamical evolution of physical profiles assuming spherical and non-spherical wind of the same total injected wind luminosity encountering with spherical fallback accretion at $t = 0$, 8.86 and 19.31 ms. Here the out- to inflow luminosity ratio $\zeta = 0.004$. The top, middle and bottom panel show the velocity, density and pressure profile, respectively.

5.2.3 2-D relativistic hydrodynamics study with quasi-spherical fallback accretion

In this section, we fix the wind luminosity to be isotropic and constant, while putting an perturbation to the fallback accretion, which is characterized by its amplitude Δ and periodicity N:

$$\dot{M}_{\mathrm{fb},\theta} = k\dot{M}_{\mathrm{fb}}(1 + \Delta\sin(N\theta)) \tag{5.38}$$

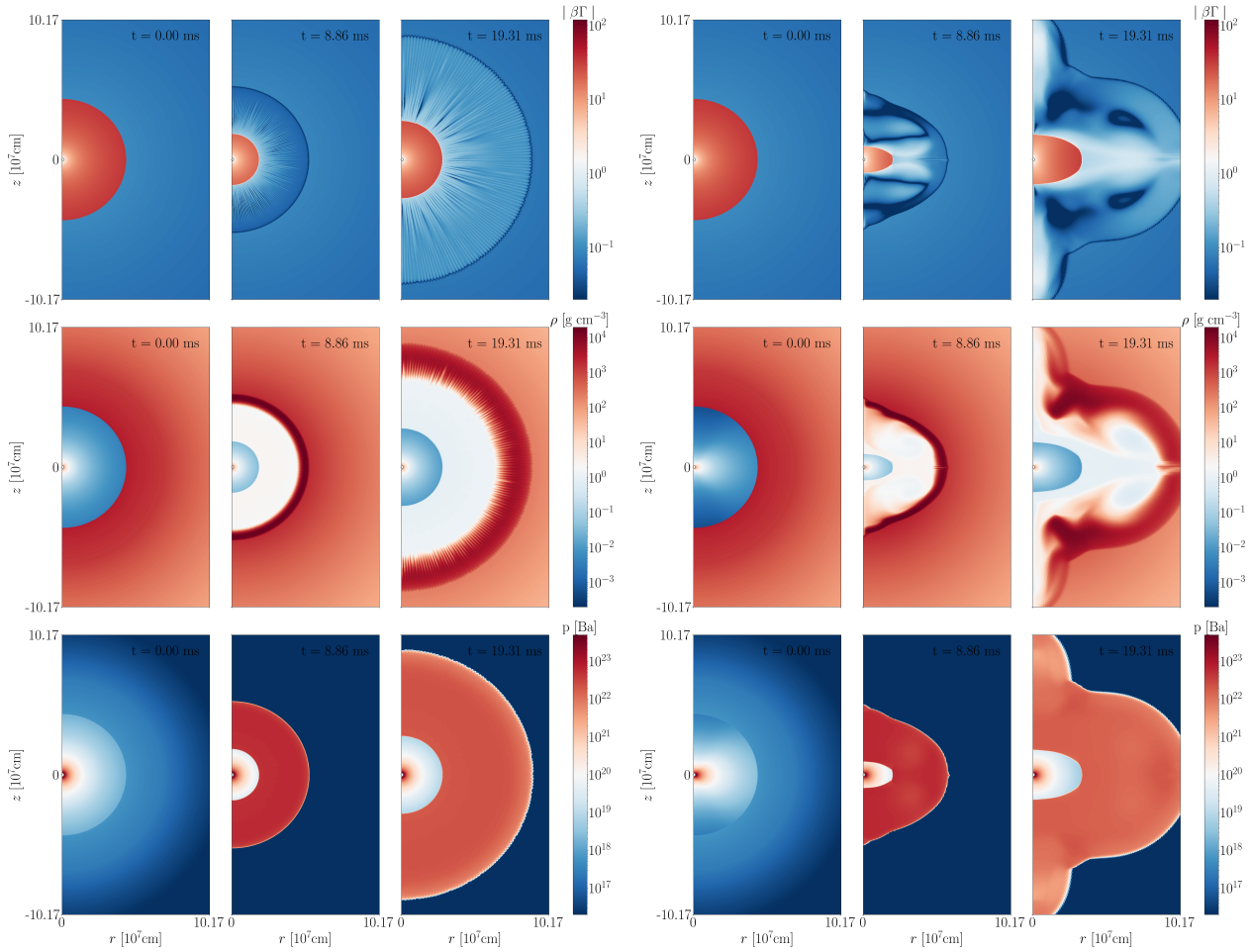

(a) $L = \text{const}$ (b) $L \propto (0.1 + \sin^4\theta)$

Figure 5.5: Comparison between dynamical evolution of physical profiles assuming spherical and non-spherical wind of the same total injected wind luminosity encountering with spherical fallback accretion at $t = 0$, 8.86 and 19.31 ms. Here the out- to inflow luminosity ratio $\zeta = 0.05$. The top, middle and bottom panel show the velocity, density and pressure profile, respectively.

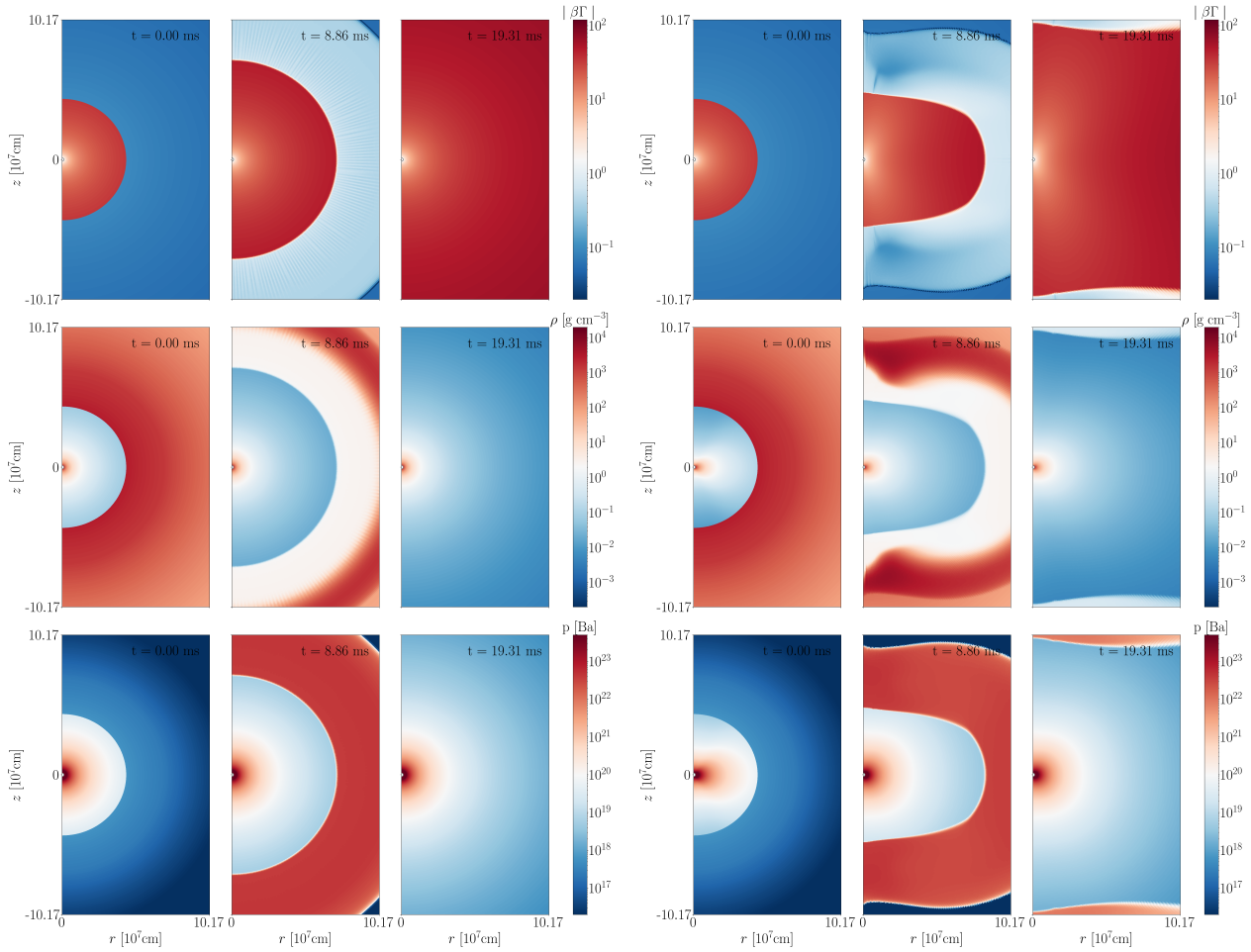

(a) $L = \text{const}$ (b) $L \propto (0.1 + \sin^4\theta)$

Figure 5.6: Comparison between dynamical evolution of physical profiles assuming spherical and non-spherical wind of the same total injected wind luminosity encountering with spherical fallback accretion at $t = 0$, 8.86 and 19.31 ms. Here the out- to inflow luminosity ratio $\zeta = 1$. The top, middle and bottom panel show the velocity, density and pressure profile, respectively.

where $\dot{M}_{\rm fb}$ stands for the total mass accretion rate shown in Eq.(2.4), and k is the coefficient for maintaining the total mass accretion rate

$$k = \frac{1}{2\pi \int_0^{\pi} (1 + \Delta \sin(N\theta) \sin\theta d\theta}, \tag{5.39}$$

which is $\sim 1/4\pi$ with N increasing. Here we set the fiducial value of Δ and N in the testing cases as shown in Table. 5.2.

parameter	notation	value
amplitude of perturbation	Δ	0.01, 0.1, 0.5
periodicity of perturbation	N	10

Table 5.2: Run parameters in 2-D testing cases with quasi-spherical fallback accretion

Under this initial setting, the boundary conditions (see Eqs.(5.9)-(5.16) the one both for the inner and outer boundary condition on θ direction and Eqs.(2.22)-(2.27) and (5.17)-(5.18) for the inner boundary condition on radius direction) shall remain unchanged except the outer boundary condition on radius direction :

$$v_{\rm fb}(r_{\rm out}, \theta) = -\sqrt{\frac{2GM_*}{r_{\rm out}}}, \tag{5.40}$$

$$v_\theta(r_{\rm out}, \theta) = 0, \tag{5.41}$$

$$\rho_{\rm fb}(r_{\rm out}, \theta) = \frac{\dot{M}_{{\rm fb},\theta}}{r_{\rm out}^2 \left| v_{\rm fb}\left(r_{\rm out}, \theta\right)\right|}, \tag{5.42}$$

$$p_{\rm fb}(r_{\rm out}, \theta) = k_{\rm fb} \rho_{\rm fb}(r_{\rm out}, \theta)^{\gamma}. \tag{5.43}$$

where the coefficient $k_{\rm fb}$ is given by fixing the sound velocity at the outer edge of the unshocked fallback region as $c_{\rm s} \sim 10^{-3}c$. The corresponding physical profiles in the ghost cell can be determined as follows:

$$v_{\rm r}{}^{iu+i,j,k} = v_{\rm r}{}^{iu,j,k} \left(\frac{r_{iu}}{r_{iu+i}}\right)^{\frac{1}{2}}, \tag{5.44}$$

$$v_\theta{}^{iu+i,j,k} = 0, \tag{5.45}$$

$$\rho^{iu+i,j,k} = \rho^{iu,j,k} \left(\frac{r_{iu}}{r_{iu+i}}\right)^{\frac{3}{2}(l+1)}, \tag{5.46}$$

$$p^{iu+i,j,k} = p^{iu,j,k} \left(\frac{\rho^{iu+i,j,k}}{\rho^{iu,j,k}}\right)^{\gamma}. \tag{5.47}$$

Where i loops from 1 to the number of ghost cells $N_{\rm ngh}$, and iu stands for the outer most cell else than the ghost cells at the outer boundary.

Given the same numerical scheme described in Chap. 5.2.2, we investigate the range of the parameters shown in Table 5.1 and 5.2. The results are shown in Fig. 5.7, 5.8 and 5.9.

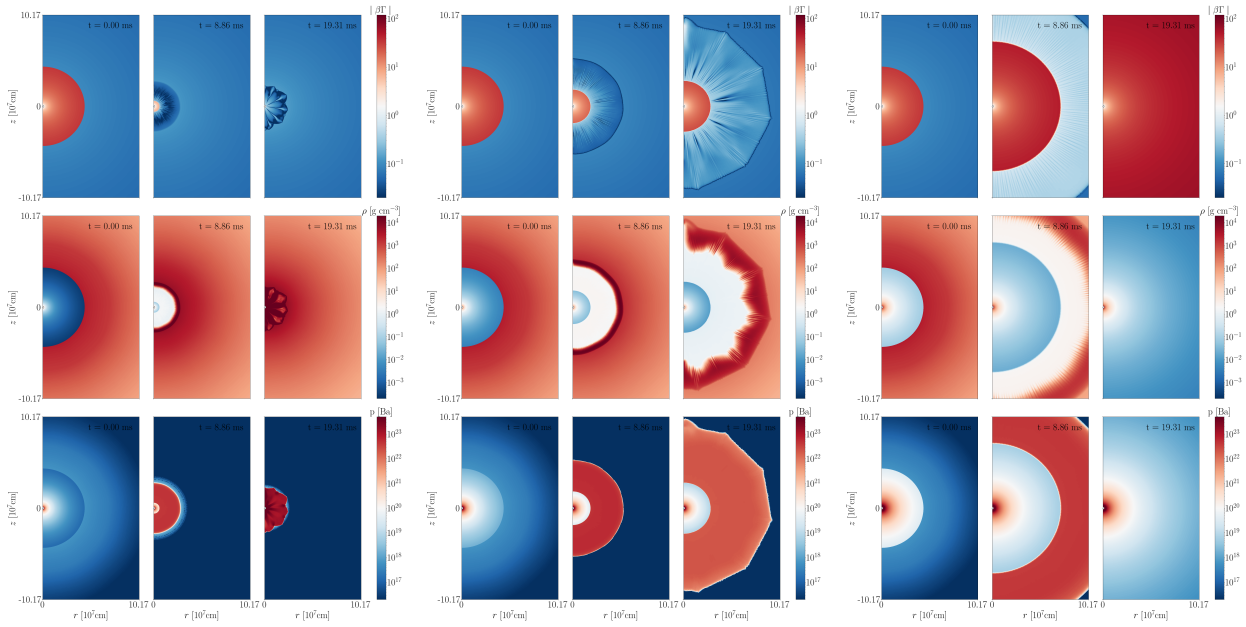

(a) $\zeta = 0.004$ (b) $\zeta = 0.05$ (c) $\zeta = 1$

Figure 5.7: Dynamical evolution of physical profiles with out- to inflow luminosity ratio $\zeta = 0.004$ (see the left panel), 0.05 (see the central panel) and 1 (see the right panel) assuming quasi-spherical fallback accretion with perturbation amplitude $\Delta = 0.01$. The snapshot are taken at $t = 0$, 8.86 and 19.31 ms. The top, middle and bottom panel show the velocity, density and pressure profile, respectively.

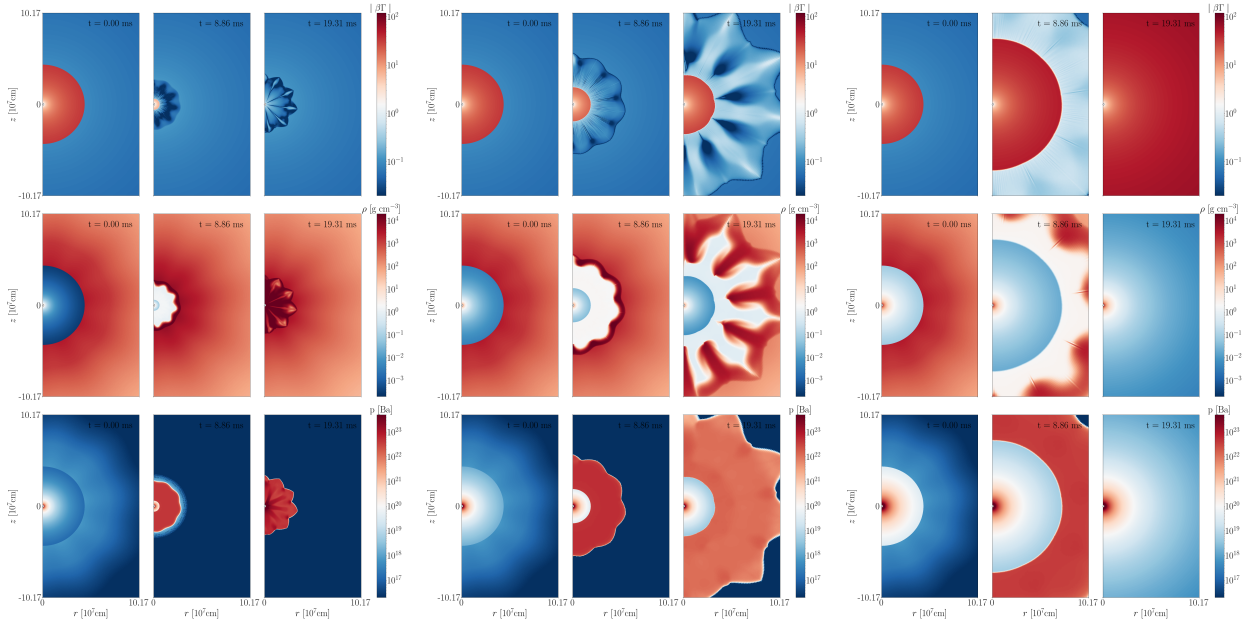

(a) $\zeta = 0.004$ (b) $\zeta = 0.05$ (c) $\zeta = 1$

Figure 5.8: Dynamical evolution of physical profiles with out- to inflow luminosity ratio $\zeta = 0.004$ (see the left panel), 0.05 (see the central panel) and 1 (see the right panel) assuming quasi-spherical fallback accretion with perturbation amplitude $\Delta = 0.1$. The snapshot are taken at $t = 0$, 8.86 and 19.31 ms. The top, middle and bottom panel show the velocity, density and pressure profile, respectively.

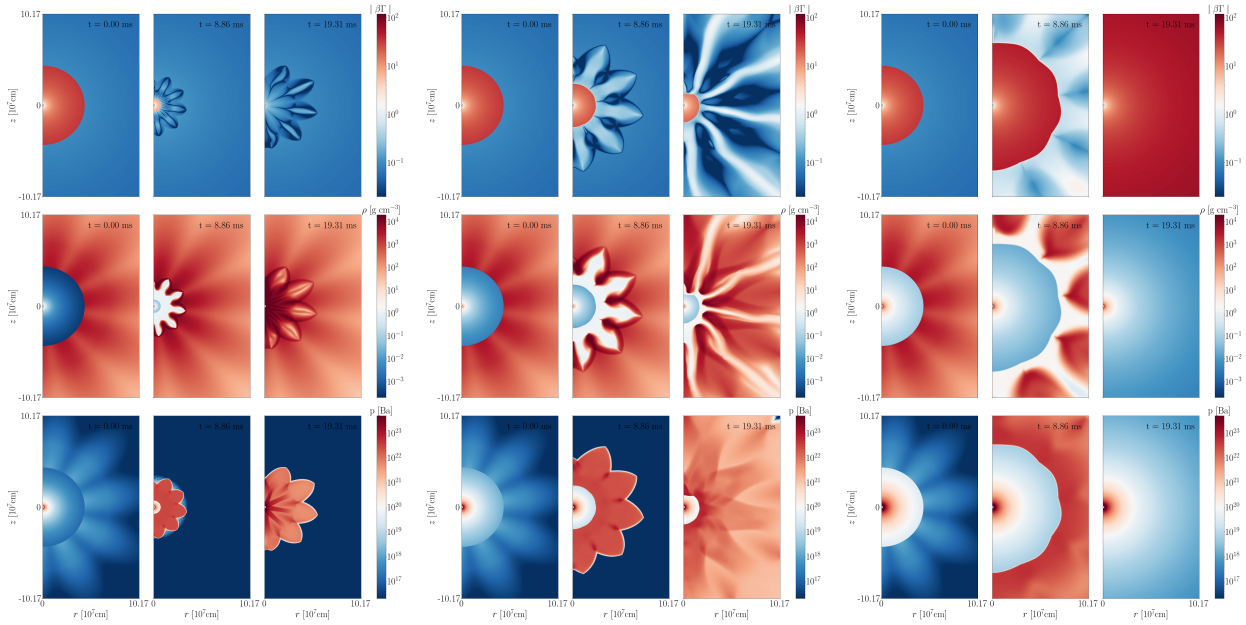

(a) $\zeta = 0.004$ (b) $\zeta = 0.05$ (c) $\zeta = 1$

Figure 5.9: Dynamical evolution of physical profiles with out- to inflow luminosity ratio $\zeta = 0.004$ (see the left panel), 0.05 (see the central panel) and 1 (see the right panel) assuming quasi-spherical fallback accretion with perturbation amplitude $\Delta = 0.5$. The snapshot are taken at $t = 0$, 8.86 and 19.31 ms. The top, middle and bottom panel show the velocity, density and pressure profile, respectively.

5.2.4 How much supernova fallback can invade down to the newborn pulsar wind?

In the 2-D RHD simulations, we found that the condition for the fallback accretion to invade down to the near NS surface region can be marked as the significantly changing of mass enclosed between NS radius R_* and light cylinder radii $r_{\rm lc}$ (see Eq.(1.13)) instead of $r_{\rm fb,min} \sim R_*$ in one-dimensional cases, since the minimum fallback radius $r_{\rm fb,min}$ cannot be defined after introducing the non-spherical effects. The enclosed mass between $r_{\rm lc}$ and R_* in cases mentioned in Secs. 5.2.2 and 5.2.3 can be crafted in Fig. 5.10 with fixing the rotation period of central NS P_i. The results are briefly summarized as follows:

1) The shocked fallback matter successfully invades down to the magnetosphere marked by light cylinder radii $r_{\rm lc}$ either when the out- to inflow luminosity ratio ζ decreases (which is also a conclusion from our 1-D study) or the non-spherical perturbation is introduced in either outflow or inflow region.

2) The time where the invading mass peaks can be roughly estimated as the fallback time scale $t_{\rm fb}$ (see Eq.(2.15)).

3) The time where the enclosed mass drop down to its initial value $t_{\rm hd}$ can be estimated as $\sim 10 t_{\rm fb}$ regardless of the choice of light cylinder radii $r_{\rm lc}$ in the intense fallback limit (see the left column of 5.10). Comparing it to the intermediate case with $t_{\rm hd} \sim t_{\rm fb}$ (see the central column of 5.10), one can see that the reason behind these two kinds of situation

are basically different: as for the former cases, it is due to the decreasing of mass accretion rate with respect to time (see Eq.(2.4)); while for the latter one, it is because that the fallback inflow is repulsed by the outflow before reaching the surface. Through which we can state a new criterion to determine the $\zeta_{\rm min}$ and $\zeta_{\rm cri}$ mainly based on the time evolution of enclosed mass $M_{\rm enclose}(t)$: cases with the decaying time scale $t_{\rm hd} \sim 10t_{\rm fb}$ stand for successfully invading ones ($\zeta < \zeta_{\rm min}$), $t_{\rm hd} \sim t_{\rm fb}$ for the invading-then-expanding ones ($\zeta_{\rm min} < \zeta < \zeta_{\rm cri}$), while constant $M_{\rm enclose}(t)$ (or $t_{\rm hd} = 0$) stands for the monotonically expanding ones ($\zeta > \zeta_{\rm cri}$).

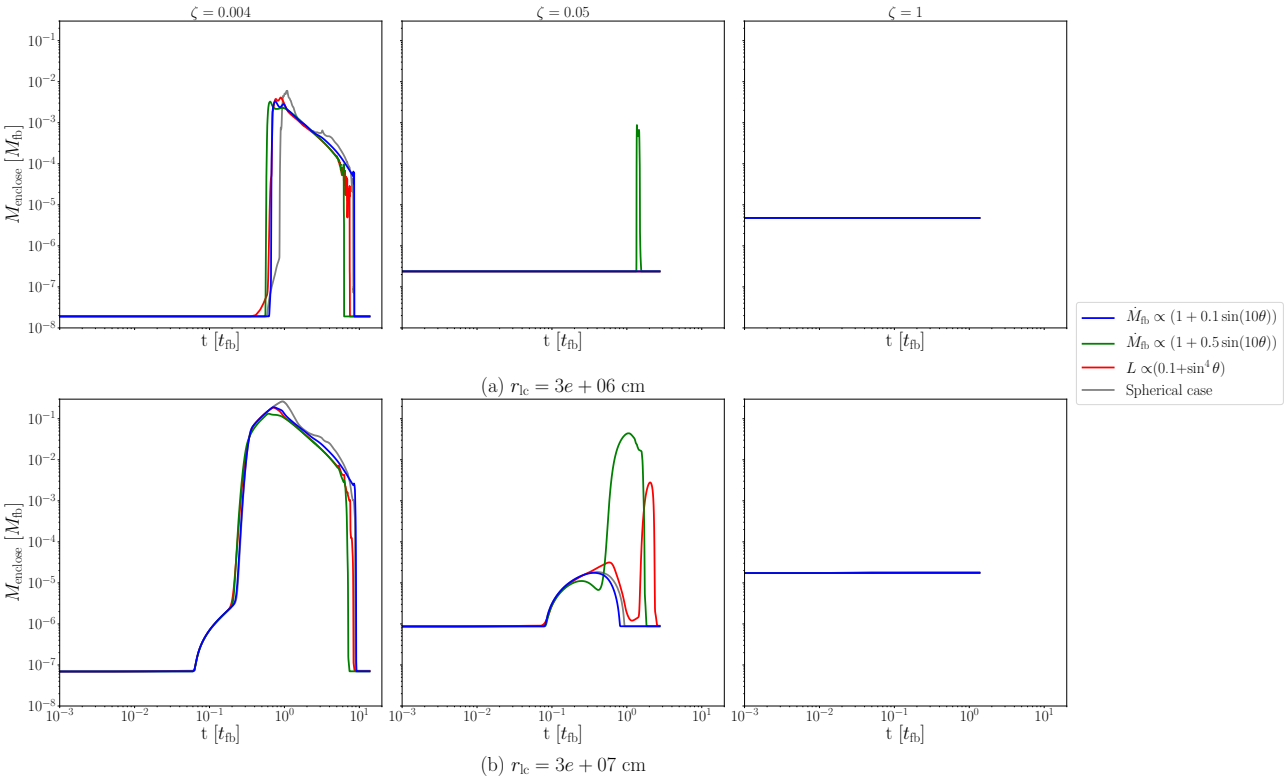

(a) $r_{\rm lc} = 3e + 06$ cm

(b) $r_{\rm lc} = 3e + 07$ cm

Figure 5.10: Time evolution of enclosed mass between NS radius R_* and light cylinder radii $r_{\rm lc}$ for the central NS with non-spherically injected outflow & spherical fallback inflow (see the red lines in both rows for different light cylinder radii $r_{\rm lc}$), spherical injected outflow & quasi-spherical fallback inflow (see the blue ($\Delta = 0.1$) and green ($\Delta = 0.5$) solid lines in both rows for different light cylinder radii $r_{\rm lc}$), and spherical injected outflow & fallback inflow (see the grey solid line) of the same out- to inflow luminosity ratio ζ. The cases with terminal Lorentz factor of outflow $\Gamma_\infty = 100$ and out- to inflow luminosity ratio $\zeta = 0.004, 0.05, 1$ under $r_{\rm enc} = 4.5 \times 10^7$ cm are shown in the left, central and right panel, respectively. The enclosed mass and simulation time are normalized with total fallback mass $M_{\rm fb}$ and fallback time scale $t_{\rm fb}$, respectively.

For future perspectives, we will first enlarge the 2-D RHD simulation domain with increasing the resolution to ensure the convergence of the results, and carefully investigate the parameter dependence of $\zeta_{\rm min}$ and $\zeta_{\rm cri}$ (e.g., the encounter radius $r_{\rm enc}$) as well as what we have done for 1-D RHD study; we will be especially interested in whether their parameter dependence still remain unchanged, which basically means that the condition for the fallback accretion to reach down to the near NS surface region is sorely determined by the energy equilibrium of the out- and inflow system, regardless of the multi-dimensional effects. Afterwards we will move on to

the 2-D RMHD studies, where a sanity check for the outflow luminosity numerically generated by the rotating dipole radiation in the form given by Tchekhovskoy et al. (2013) will be carried out before the long-term simulations that run until the system settles down and reaches the end stage. Eventually we want to extend the results to 3-D RMHD simulations, and make the whole physical picture more realistic through connecting the initial condition for our simulations with the post supernova explosion stage. The results will be compared with observational facts such as the birth rate, progenitor mass, the supernova and early pulsar wind nebula emission of each category of NSs.

Appendix A

Thin shell model for the shocked fallback matter

To explain the dependence of the minimum fallback radius on the out- to inflow energy flux ratio (see Fig. 3.4 and Fig. 3.5) shown in Sec. 3, a simplified thin-shell model describing the dynamics of supernova fallback confronting with an energy injection from the central source will be constructed in this chapter.

Considering that the shocked fallback matter can be modeled as a shell with a velocity of $v_{\rm fb}$ and a mass of $M_{\rm fb}$ at $r = r_{\rm fb}$, the governing equations including mass, momentum, and energy conservation can be described as

$$\frac{dM_{\rm fb}}{dt} = -4\pi r_{\rm fb}^2 \rho (v - v_{\rm fb}), \tag{A.1}$$

$$\frac{d(M_{\rm fb} v_{\rm fb})}{dt} = 4\pi r_{\rm fb}^2 p - \dot{M}_{\rm fb,ini}\,(v - v_{\rm fb}) - \frac{G M_* M_{\rm fb}}{r_{\rm fb}^2}, \tag{A.2}$$

and

$$3\frac{d}{dt}(pV) + p\frac{dV}{dt} = L \tag{A.3}$$

with

$$v = \sqrt{2GM_*/r_{\rm fb}}, \tag{A.4}$$

$$\rho = \dot{M}_{\rm fb,ini} / \left(4\pi r_{\rm fb}^2 v\right) \tag{A.5}$$

and

$$V = 4\pi r_{\rm fb}^3/3. \tag{A.6}$$

Note that we take the non-relativistic form of hydrodynamics equations here for describing the dynamics of the shocked fallback shell, since the velocity of the shocked region is well below the speed of light; and the outflow luminosity and mass fallback rate are considered to be constant during the evolution.

A.1 Asymptotic solutions for small t

First we will consider the asymptotic solutions for small t. The velocity, mass, and pressure of the thin shell can be expressed as

$$v_{\rm fb}(t) = v_{\rm fb,0} + at, \tag{A.7}$$

$$M_{\rm fb}(t) = \dot{M}_{\rm s} t + \ddot{M}_{\rm s} t^2/2, \tag{A.8}$$

$$p(t) = L/(4\pi r_{\rm enc}^2 c) + \dot{p}t + \ddot{p}t^2/2, \tag{A.9}$$

respectively, with a being the acceleration of the fallback shell. The initial conditions are set as $r_{\rm fb,0} = r_{\rm enc}$, $v_{\rm fb}(t) = v_{\rm fb,0}$, $M_{\rm fb,0} = 0$, and $4\pi r_{\rm enc}^2 p_0 = L/c$; where $v_{\rm fb,0}$, $\dot{M}_{\rm s}$ and a can be obtained by substituting Eq. (A.7), (A.8), and (A.9) into Eq. (A.1), (A.2), and (A.3) as

$$v_{\rm fb,0} = \sqrt{\frac{2GM}{r_{\rm enc}}} \left(\sqrt{\zeta/\zeta_{\rm cri}} - 1 \right), \tag{A.10}$$

$$\dot{M}_{\rm s} = \dot{M}_{\rm fb,\ i} \sqrt{\zeta/\zeta_{\rm cri}}, \tag{A.11}$$

$$a = \frac{c^4 \left(5(1-\zeta/\zeta_{\rm cri}) + 7\sqrt{\zeta/\zeta_{\rm cri}} - 7 + 2\sqrt{y\zeta/\zeta_{\rm cri}} \right)}{12GMy^2}, \tag{A.12}$$

with

$$y = \frac{c^2 r_{\rm enc}}{2GM}. \tag{A.13}$$

What we can learn from Eq. (A.10) is that the shocked matter shell initially expands ($v_{\rm fb,0} > 0$) while the factor $\zeta/\zeta_{\rm cri}$ is greater than unity, which is consistent with the numerical result shown in Eq. 3.1; otherwise the shell reaches the minimum fallback radii $r_{\rm fb,min}$ at time $t = t_{\rm min} = -v_{\rm fb,0}/a$ as long as $\zeta/\zeta_{\rm cri}$ is not significantly smaller than unity. In this case, the minimum fallback radius can be estimated as

$$r_{\rm fb,min}(x,y) = \frac{2GMy}{c^2} \times \left[\frac{8\left(\zeta/\zeta_{\rm cri} - 1\right) - 13\sqrt{\zeta/\zeta_{\rm cri}} + 13 - 2\sqrt{y\zeta/\zeta_{\rm cri}}}{5\left(\zeta/\zeta_{\rm cri} - 1\right) - 7\sqrt{\zeta/\zeta_{\rm cri}} + 7 - 2\sqrt{y\zeta/\zeta_{\rm cri}}} \right], \tag{A.14}$$

which is also consistent with the numerically obtained minimum fallback radius $r_{\rm fb,min}$ for $\zeta/\zeta_{\rm cri} \sim 1$.

A.2 Long-term behavior

Here we derive the solution that can be applied to a relatively large t. In the cases with out-to inflow luminosity ratio $\zeta < \zeta_{\rm cri}$, the thin shell initially contracts ($v_{\rm fb,0} < 0$) and reaches the innermost radius $r_{\rm fb,min}$ at $t = t_{\rm min}$, $v_{\rm fb} = 0$. The critical condition is achieved where the thin

shell marginally becomes gravitationally unbound, i.e.,

$$dv_{\rm fb}/dt = 0 \,{\rm at}\, t = t_{\rm min}, \tag{A.15}$$

which, by substituting these conditions into Eq. (A.1) and (A.2), leads to

$$4\pi r_{\rm fb,min}^2 p = \dot{M}_{\rm fb,i}\sqrt{2GM/r_{\rm fb,min}} + \frac{GM_* M_{\rm fb}}{r_{\rm fb,min}^2}. \tag{A.16}$$

Where the pressure term in the left hand side of the equation can be evaluated by integrating Eq. (A.3) over time as

$$r_{\rm fb,min}^4 p = r_{\rm enc}^4 p_0 + \frac{L}{4\pi}\int_0^{t_{\rm min}} dt' r_{\rm fb}(t'). \tag{A.17}$$

The minimum fallback radius can be thus obtained by substituting Eq. (A.17) to Eq. (A.16) as

$$r_{\rm fb,min} = r_{\rm enc}[\zeta f(t_{\rm min}) - g(t_{\rm min})]^{2/3}\left(\frac{c^2 r_{\rm enc}}{2GM}\right)^{1/3}, \tag{A.18}$$

with

$$f(t_{\rm min}) = 1 + \frac{c\int_0^{t_{\rm min}} dt' r_{\rm fb}(t')}{r_{\rm enc}^2}, \tag{A.19}$$

$$g(t_{\rm min}) = \frac{GM_* M_{\rm fb}(t_{\rm min})}{c r_{\rm enc}^2 \dot{M}_{\rm fb,i}} \tag{A.20}$$

Regardless of the fact that the exact values of $f(t_{\rm min})$, $g(t_{\rm min})$, and $r_{\rm fb,min}$ shall be obtained by directly solving Eq. (A.1), (A.2), and (A.3), they can be approximated as

$$f(t_{\rm min}) \approx c t_{\rm fb}/r_{\rm enc} \tag{A.21}$$

and

$$g(t_{\rm min}) \approx GM_* t_{\rm fb}/c{r_{\rm enc}}^2 \tag{A.22}$$

as long as $t_{\rm min} \lesssim t_{\rm fb}$. The critical out- to inflow luminosity ratio that gives $r_{\rm fb,min} \to 0$ can be roughly estimated as $\zeta_{\rm min} \approx g(t_{\rm min})/f(t_{\rm min}) \approx GM_*/c^2 r_{\rm enc}$ from Eq. (A.18), which is consistent with the numerical results and can be interpreted as follows; $\zeta f(t)$ and $g(t)$ represent the time-integrated outflow luminosity injected to the thin shell and the work exerted by the gravitational force to the thin shell, respectively. The critical out- to inflow luminosity ratio $\zeta_{\rm min}$ marks the fallback matter to invade down to the near NS surface corresponds to the case where these two energy components become comparable at $t \approx t_{\rm fb}$.

This thin-shell model can well describe the dependence of the minimum fallback radius on the out- to inflow energy flux ratio shown in Sec. 3 mainly due to the validity of non-relativistic form of hydrodynamics equations (especially the momentum and energy conservation laws) in the thin shocked region, where its velocity is non-relativistic during the early stage of the in- and outflow encounter regardless of the relativistic outflow velocity. A breakdown of this point can lead to the deviation between the one predicted by the analytical model and numerical simulation; for example, if we consider extra source term in the energy equation (e.g., neutrino cooling), the effects of magnetic field especially in the near NS surface region where the plasma β is well below the unity, or a larger simulation box in which the accretion shock may not be regarded as a thin shell any more.

Appendix B

Rayleigh-Taylor instability on the inflow-outflow boundary

As introduced in Sec. 3, our physical set-ups at the encounter radius can be locally simplified as Fig. B.1, where Γ, ρ and h stand for the Lorentz factor, density and enthalpy at both sides of $r_{\rm enc}$ (see the black dashed line), respectively; and the parameters with prim represent the property of the fallback matter.

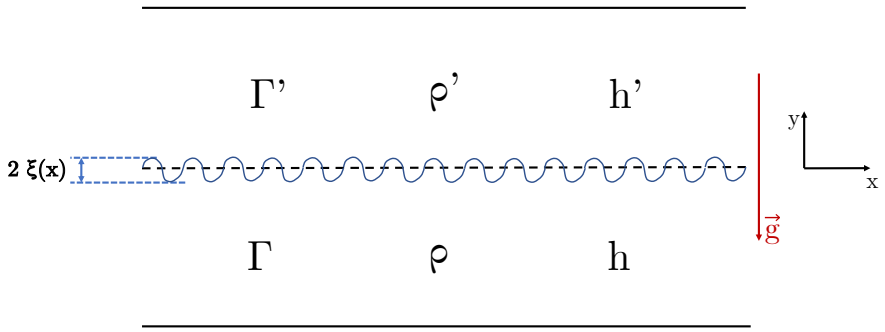

Figure B.1: Simplified local physical setups at the encounter radius

Here we consider a small perturbation ξ(x) at the encounter radius $r_{\rm enc}$ (see Fig. B.1) with the form of simple harmonics

$$\xi(\mathrm{x}) \propto \exp(i(\hat{k}\hat{r} - \omega t)) \tag{B.1}$$

where the governing equations of this system can be written as:

$$\Gamma\frac{\partial\delta\rho}{\partial t} + \delta v_y\frac{\partial(\Gamma\rho)}{\partial y} = 0, \tag{B.2}$$

$$\frac{\partial\delta v_x}{\partial x} + \frac{\partial\delta v_y}{\partial y} = 0, \tag{B.3}$$

$$\Gamma^2 \rho h \frac{\partial \delta v_x}{\partial t} = -\frac{\partial \delta p}{\partial x}, \tag{B.4}$$

$$\Gamma^2 \rho h \frac{\partial \delta v_y}{\partial t} = -\frac{\partial \delta p}{\partial y} - \Gamma^2 \left(\delta\rho + \frac{\gamma}{\gamma - 1} \frac{\delta p}{c^2} \right) g, \tag{B.5}$$

$$\frac{1}{p} \left(\frac{\partial \delta p}{\partial t} + \delta v_y \frac{\partial p}{\partial y} \right) - \frac{\gamma}{\rho} \left(\frac{\partial \delta \rho}{\partial t} + \delta v_y \frac{\partial \rho}{\partial y} \right) = 0, \tag{B.6}$$

which gives the oscillation frequency ω in Eq.(B.1) through following assumptions

1) Both the inflow and outflow can be regarded as incompressible:

$$\frac{\partial}{\partial t}(\Gamma\rho) + \mathbf{v}\nabla(\Gamma\rho) = 0 \tag{B.7}$$

2) The system is initially in hydrostatic equilibrium on this plane:

$$\nabla p + \Gamma^2 \rho h g = 0 \tag{B.8}$$

3) Only a thin layer of flow at both sides of encounter radius are considered, thus the Lorentz factor Γ and density ρ profiles are uniform for inflow and outflow.

4) Angular frequency of oscillation ω is constant

5) Every physical quantity Q together with its derivative towards time/space ($\partial_t Q$ and $\partial_i Q$) vanish at $r \to \infty$

as

$$\omega^2 = -gk \frac{\Gamma'^2 \rho' h'_0 - \Gamma^2 \rho h_0}{\Gamma'^2 \rho' h'_0 + \Gamma^2 \rho h_0} \tag{B.9}$$

where k is the wave number of the perturbation, g is the local gravitational acceleration; and

$$h'_0 = 1 + \frac{\gamma^2 p'_0}{(\gamma - 1)\rho' c^2}, \tag{B.10}$$

$$h_0 = 1 + \frac{\gamma^2 p_0}{(\gamma - 1)\rho c^2}, \tag{B.11}$$

with p'_0 and p_0 to be the pressure of the inflow and outflow at their interface, which initially will be the encounter radius $r_{\rm enc}$. Instability happens when $\omega^2 < 0$, or

$$\Gamma'^2 \rho' h'_0 > \Gamma^2 \rho h_0 \tag{B.12}$$

which has been satisfied especially for the contracting phase in parameter space with $\zeta \lesssim \zeta_{\rm cri}$ that we are most interested in.

Bibliography

Abdo, A. A., Ackermann, M., Ajello, M., et al. 2010, ApJ, 708, 1254

Akiyama, S., Wheeler, J. C., Meier, D. L., & Lichtenstadt, I. 2003, ApJ, 584, 954

Alpar, M. A., Cheng, A. F., Ruderman, M. A., & Shaham, J. 1982, Nature, 300, 728

Arons, J. & Scharlemann, E. T. 1979, ApJ, 231, 854

Backer, D. C. 1970a, Nature, 228, 1297

Backer, D. C. 1970b, Nature, 228, 42

Backer, D. C., Kulkarni, S. R., Heiles, C., Davis, M. M., & Goss, W. M. 1982, Nature, 300, 615

Beniamini, P., Hotokezaka, K., van der Horst, A., & Kouveliotou, C. 2019, MNRAS, 487, 1426

Bethe, H. A. 1990, Reviews of Modern Physics, 62, 801

Burkardt, J. 2020, SPLINE, a C++ code which constructs and evaluates spline functions

Burrows, A. 1988, ApJ, 334, 891

Burrows, A. 1990, Annual Review of Nuclear and Particle Science, 40, 181

Cea, P. 2006, A&A, 450, 199

Chauvin, M., Florén, H. G., Friis, M., et al. 2017, Scientific Reports, 7, 7816

Chen, K. & Ruderman, M. 1993, ApJ, 402, 264

Cheng, K. S., Ho, C., & Ruderman, M. 1986, ApJ, 300, 500

Chevalier, R. A. 1989, ApJ, 346, 847

Duncan, R. C. & Thompson, C. 1992, ApJ, 392, L9

Endeve, E., Cardall, C. Y., Budiardja, R. D., et al. 2012, ApJ, 751, 26

Enoto, T., Kisaka, S., & Shibata, S. 2019, Reports on Progress in Physics, 82, 106901

Enoto, T., Sasano, M., Yamada, S., et al. 2014, ApJ, 786, 127

Enoto, T., Shibata, S., Kitaguchi, T., et al. 2017, ApJS, 231, 8

Ertl, T., Janka, H. T., Woosley, S. E., Sukhbold, T., & Ugliano, M. 2016a, ApJ, 818, 124

Ertl, T., Ugliano, M., Janka, H.-T., Marek, A., & Arcones, A. 2016b, ApJ, 821, 69

Ferrario, L., de Martino, D., & Gänsicke, B. T. 2015, Space Science Reviews, 191, 191

Fesen, R. A., Kremer, R., Patnaude, D., & Milisavljevic, D. 2012, AJ, 143, 27

Gill, R. & Heyl, J. 2007, MNRAS, 381, 52

Goldreich, P. & Julian, W. H. 1969, ApJ, 157, 869

Goldreich, P. & Reisenegger, A. 1992, ApJ, 395, 250

Goldreich, P. & Weber, S. V. 1980, ApJ, 238, 991

Gotthelf, E. V. & Halpern, J. P. 2009, ApJ, 695, L35

Gotthelf, E. V., Perna, R., & Halpern, J. P. 2010, ApJ, 724, 1316

Gruzinov, A. 2005, Phys. Rev. Lett., 94, 021101

Hailey, C. J. & Mori, K. 2002, ApJ, 578, L133

Halpern, J. P. & Gotthelf, E. V. 2010, ApJ, 709, 436

Hamil, O., Stone, J. R., Urbanec, M., & Urbancová, G. 2015, Phys. Rev. D, 91, 063007

Harding, A. K. & Lai, D. 2006, Reports on Progress in Physics, 69, 2631

Heger, A., Fryer, C. L., Woosley, S. E., Langer, N., & Hartmann, D. H. 2003, ApJ, 591, 288

Hewish, A., Bell, S. J., Pilkington, J. D. H., Scott, P. F., & Collins, R. A. 1968, Nature, 217, 709

Heyl, J. S. & Kulkarni, S. R. 1998, ApJ, 506, L61

Ho, W. C. G. & Heinke, C. O. 2009, Nature, 462, 71

Hotokezaka, K., Kiuchi, K., Kyutoku, K., et al. 2013, Phys. Rev. D, 88, 044026

Janka, H. T., Langanke, K., Marek, A., Martínez-Pinedo, G., & Müller, B. 2007, Phys. Rep., 442, 38

Janka, H. T., Wongwathanarat, A., & Kramer, M. 2021, arXiv e-prints, arXiv:2104.07493

Kaspi, V. M. 2007, Ap&SS, 308, 1

Kaspi, V. M. & Beloborodov, A. M. 2017, ARA&A, 55, 261

Kaspi, V. M., Gavriil, F. P., Woods, P. M., et al. 2003a, ApJ, 588, L93

Kaspi, V. M., McLaughlin, M. A., Stairs, I. H., et al. 2003b, in AAS/High Energy Astrophysics Division, Vol. 7, AAS/High Energy Astrophysics Division #7, 20.09

Keane, E. F. & Kramer, M. 2008, MNRAS, 391, 2009

Kouveliotou, C., Dieters, S., Strohmayer, T., et al. 1998, Nature, 393, 235

Kouveliotou, C., Fishman, G. J., Meegan, C. A., et al. 1994, Nature, 368, 125

Kuiper, L., Hermsen, W., Walter, R., & Foschini, L. 2003, A&A, 411, L31

Lattimer, J. M. 2012, Annual Review of Nuclear and Particle Science, 62, 485

Lattimer, J. M. & Prakash, M. 2007, Phys. Rep., 442, 109

Lyubarskii, Y. E. 1992, A&A, 265, L33

Manchester, R. N., Hobbs, G. B., Teoh, A., & Hobbs, M. 2005, AJ, 129, 1993

Metzger, B. D., Beniamini, P., & Giannios, D. 2018, ApJ, 857, 95

Mignone, A. & Bodo, G. 2005, MNRAS, 364, 126

Mignone, A., Ugliano, M., & Bodo, G. 2009, MNRAS, 393, 1141

Mori, K., Gotthelf, E. V., Zhang, S., et al. 2013, ApJ, 770, L23

Morini, M., Robba, N. R., Smith, A., & van der Klis, M. 1988, ApJ, 333, 777

Morris, D. J., Hobbs, G., Lyne, A. G., et al. 2002, MNRAS, 335, 275

Muslimov, A. & Page, D. 1995, ApJ, 440, L77

Nobili, L., Turolla, R., & Zane, S. 2008, MNRAS, 389, 989

Nomoto, K., Sparks, W. M., Fesen, R. A., et al. 1982, Nature, 299, 803

Olausen, S. A. & Kaspi, V. M. 2014, ApJS, 212, 6

Olausen, S. A., Zhu, W. W., Vogel, J. K., et al. 2013, ApJ, 764, 1

Ostriker, J. P. & Gunn, J. E. 1969, ApJ, 157, 1395

Pacini, F. 1967, Nature, 216, 567

Pandolfi, M. & D'Ambrosio, D. 2001, Journal of Computational Physics, 166, 271

Parfrey, K., Spitkovsky, A., & Beloborodov, A. M. 2016, ApJ, 822, 33

Pavlov, G. G. & Luna, G. J. M. 2009, ApJ, 703, 910

Pétri, J. & Kirk, J. G. 2005, ApJ, 627, L37

Potekhin, A. Y., De Luca, A., & Pons, J. A. 2015, Space Sci. Rev., 191, 171

Roe, P. L. 1986, Annual Review of Fluid Mechanics, 18, 337

Ruderman, M. A. & Sutherland, P. G. 1975, ApJ, 196, 51

Rutledge, R. E., Fox, D. B., & Shevchuk, A. H. 2008, ApJ, 672, 1137

Sedrakian, A. & Cordes, J. M. 1998, ApJ, 502, 378

Seward, F. D., Charles, P. A., & Smale, A. P. 1986, ApJ, 305, 814

Shabaltas, N. & Lai, D. 2012, ApJ, 748, 148

Shapiro, S. L. & Teukolsky, S. A. 1983, Black holes, white dwarfs, and neutron stars : the physics of compact objects

Shevchuk, A. S. H., Fox, D. B., & Rutledge, R. E. 2009, ApJ, 705, 391

Shigeyama, T. & Kashiyama, K. 2018, PASJ, 70, 107

Slane, P., Hughes, J. P., Edgar, R. J., et al. 2001, ApJ, 548, 814

Słowikowska, A., Kanbach, G., Kramer, M., & Stefanescu, A. 2009, MNRAS, 397, 103

Spitkovsky, A. 2006, ApJ, 648, L51

Staubert, R., Trümper, J., Kendziorra, E., et al. 2019, A&A, 622, 622

Stone, J. M., Tomida, K., White, C. J., & Felker, K. G. 2020, ApJS, 249, 4

Sturrock, P. A. 1971, ApJ, 164, 529

Tchekhovskoy, A., Spitkovsky, A., & Li, J. G. 2013, MNRAS, 435, L1

Thompson, C. & Duncan, R. C. 1993, ApJ, 408, 194

Thompson, C. & Duncan, R. C. 1996, ApJ, 473, 322

Thompson, C. & Duncan, R. C. 2001, ApJ, 561, 980

Thompson, T. A., Quataert, E., & Burrows, A. 2005, ApJ, 620, 861

Torres-Forné, A., Cerdá-Durán, P., Pons, J. A., & Font, J. A. 2016, MNRAS, 456, 3813

Tsuruta, S., Sadino, J., Kobelski, A., et al. 2009, ApJ, 691, 621

Tuohy, I. & Garmire, G. 1980, ApJ, 239, L107

Ugliano, M., Janka, H.-T., Marek, A., & Arcones, A. 2012, ApJ, 757, 69

Van Leer, B. 1974, Journal of Computational Physics, 14, 361

Vasisht, G. & Gotthelf, E. V. 1997, ApJ, 486, L129

Vink, J. & Kuiper, L. 2006, MNRAS, 370, L14

Woltjer, L. 1964, ApJ, 140, 1309

Woods, P. M. & Thompson, C. 2006, Soft gamma repeaters and anomalous X-ray pulsars: magnetar candidates, Vol. 39, 547–586

Xie, Y. & Zhang, S.-N. 2019, ApJ, 880, 123

Young, P. A., Fryer, C. L., Hungerford, A., et al. 2006, ApJ, 640, 891

Zavlin, V. E., Pavlov, G. G., Sanwal, D., & Trümper, J. 2000, ApJ, 540, L25

Zhu, W. W., Kaspi, V. M., McLaughlin, M. A., et al. 2011, ApJ, 734, 44